Modelling and Control of the Piezoelectric Excitation of an Automotive Windshield for Active Noise Cancellation

Brent Patrick Laurence

Centre for Intelligent Machines
Department of Electrical & Computer Engineering
McGill University
Montreal, Canada

August 2013

A thesis submitted to McGill University in partial fulfillment of the requirements for the degree of Masters in Electrical Engineering.

2013/08/12

Abstract

In this thesis, a technique for implementing active noise control within an automotive vehicle is presented utilizing the actuation of a piezoelectrically driven windshield to create the anti-noise signal. The acoustic linearity of the power efficient speaker is also improved to match that of a traditional, high-performance cone speaker. With direct measurement of the corrupting noise signal impractical, a closed-loop feedback control system is designed to achieve both objectives simultaneously. Modelling of the plant dynamics is carried out by deterministic subspace identification on filtered empirical data of a laboratory apparatus which is scaled to match vehicular installations. A noise estimator, based on internal models of the system dynamics, generates a stream of synthetic noise measurements on which stochastic subspace identification is performed to produce periodically updated models of the plant disturbance. The spectral density estimate of the output disturbance is incorporated directly into $\mathcal{H}_\infty$ synthesis to identify an optimal feedback controller. Ambient highway noise and the window buffeting phenomenon, experienced by the driver-side passenger within the vehicle, are formulated and solved by independent optimization problems to maximize improvement of the passenger's acoustic experience.

Résumé

Dans cette thèse, une technique pour réaliser le contrôle actif du bruit dans un véhicule automobile est présentée en utilisant des actionneurs piézoélectriques qui font osciller un pare-brise pour créer le signal d'anti-bruit. L'efficacité énergétique du haut-parleur piézoélectrique est également améliorée avec la linéarité acoustique pour correspondre à celle d'un haut-parleur conique traditionnel. La mesure directe du signal de bruit étant impossible, un système de régulation par rétroaction est conçu pour atteindre les deux objectifs simultanément. La modélisation de la dynamique du système est effectuée par identification déterministe en sous-espaces sur des mesures empiriques filtrées d'un appareil de laboratoire calibré en fonction de linstallation dans un véhicule. Un estimateur de bruit, basé sur des modèles internes de la dynamique du système, génère un flux de mesures de bruit de synthèse sur lequel une identification stochastique en sous-espaces est effectuée pour produire des modèles mis à jour de manière périodique de la perturbation. L'estimation de la densité spectrale de la perturbation à la sortie est incorporée directement dans la synthèse $\mathcal{H}_\infty$ pour identifier un contrôleur rétroactif optimal. Le bruit ambiant de l'autoroute et le phénomène de turbulence causé par une fenêtre ouverte (*window buffeting*), subis par le passager du côté conducteur dans le véhicule, sont formulés et résolus par des problèmes d'optimisation indépendants afin de maximiser l'amélioration de l'expérience acoustique du passager.

Acknowledgments

I would like to sincerely thank my supervisor, Professor Benoit Boulet, for his guidance and thoughtful insights without which this thesis would not have been possible. The opportunity to take part in this research project is one for which I will be eternally grateful.

I would also like to thank the University of Windsor and Todd Deaville, Philip Grella, and Greg Rizzo at Magna International Incorporated for their generosity in providing the experimental apparatus to carry out the laboratory tests which were crucial in enabling a thorough investigation of the dynamics of piezoelectric speaker systems. The coordination of such efforts would not have been possible without the expertise of Auto21.

The resources provided by the Centre for Intelligent Machines and the Schulich Library of Science and Engineering were invaluable in facilitating this work.

I would like to thank the unconditional and persistent encouragement of my best friends and family. To my parents Cathy and Brian, brother Michael, and loving grandparents Patrick & Annette Morrissey and Muriel & Donald Laurence: thank you for your limitless love and support.

Finally, a very special thank you to Alisa Kuzmina for standing behind me with love and graceful patience: you were the light that guided me through the long tunnel to success.

Contents

List of Figures

List of Tables

List of Acronyms

ADC	Analog to Digital Converter
ANC	Active Noise Cancellation
DATAQ	Data Acquisition
DAC	Digital to Analog Converter
DSP	Digital Signal Processor
FxLMS	Filtered-x Least-Mean-Square
IMC	Internal Model Control
LFT	Linear Fractional Transformation
LMS	Least-Mean-Square
MIMO	Multiple-Input Multiple-Output
MIPS	Million Instructions Per Second
NMP	Non-Minimum Phase
OLHP	Open Left Hand Plane
SISO	Single-Input Single-Output
SPL	Sound Pressure Level
VDC	Volts of Direct Current

Chapter 1

Introduction

1.1 Background

Through the collaborative efforts of Academic Institutions across Canada and Magna International, under the sponsorship of the AUTO21 Network of Centres of Excellence, a project is initiated for the commercialization of an invention by Mats Gustavsson in the field of vehicular acoustics. With the broad objective of bettering Canada's position at the forefront of high-technology innovation in automotive manufacturing, it is the intent of this collaboration to improve the passenger experience in modern vehicles by introducing an alternative means of high-fidelity acoustics. While traditional speaker systems utilize the common speaker cone assembly to produce sound, a novel technique for acoustic excitation was developed and patented by Gustavsson [1] whereby the windshield of the vehicle is mounted to piezoelectric actuators and oscillated to generate an auditory response. The significant reductions in power consumption and space requirements are added benefits to the crisp sound produced by the invention.

Magna International, a supplier and innovator of automotive parts, sought to introduce the invention into commercial automobiles to replace elements of existing audio systems, specifically for emphasis in low-pitch audio frequency reproduction. The surface area of the front and rear windshields - the most feasible surfaces for oscillation by Gustavsson's invention - tend to favour a response under 300 Hz making them a good candidate to replace subwoofers. The wavelength of low-frequency sound necessitates the incorporation of large enclosure cavities for good amplification of sound pressure waves; this in conflict to the many design constraints in automobiles in which space is a limiting factor. Utilizing

the surface of the windshield presents an opportunity for gaining significant competitive advantage in automotive designs by eliminating the traditional subwoofer which typically consumes space in the trunk or back seat of the passenger cabin. From a design and manufacturing perspective, while the windshield specifications are typically consistent among many vehicles in a particular series, the interiors vary widely and require redesigns to incorporate the subwoofer in varying cabin configurations. By exploiting the commonality in windshields that vary little or not at all between models, the subwoofer system may be designed once and replicated among the full range of vehicles to effectively reduce both design and manufacturing costs.

1.2 System Description

The principle of operation behind the production of the acoustic response relies on the reaction of select ceramics to an applied voltage [2]. The presence of an electric field induces a net displacement in the crystal which is manifested as a tensile or compressive displacement from the nominal dimensions. When the excitation signal is applied at frequencies within the range audible to humans, between 20 Hz to 20 kHz, the rapid oscillation of the crystals is perceived as sound. An inherent limitation to this process is the low stroke length of the oscillation which, in itself, would fail to produce sufficient amplitudes for use as a speaker. Utilizing the force created by the conversion from electrical to mechanical energy, Gustavsson invented a mechanical amplification device to increase the amplitude to an order capable of producing sound pressure level (SPL) comparable to that of a subwoofer.

The piezoelectric apparatus in [1] is affixed to a windshield using a sealant and pretensioned using a series of springs to improve the acoustic response of the speaker in a process developed at Magna. Through empirical testing, Magna determined that the static compressive load experienced by the polycrystal in combination with a DC bias of approximately +85V was deemed optimal for establishing good conditions for acoustic playback. With detrimental effects caused by the application of a reversed voltage polarity, the DC offset serves to safely enable a swing of +/-80V from the bias for music production without risking damage.

With the installation of the windshield assembly in a prototype at Magna, the behaviour of the piezoelectric could be evaluated to verify feasibility of the proposed project. Todd Deaville led the design of the acoustic subsystem at Magna and constructed a full-scale

model of the interior automotive front seat cabin complete with a windshield and four actuators to oscillate in phase for consistent displacement across the entire surface area of the glass.

Through empirical tests and a general mandate for passenger experience improvement, several critical issues are stated. The issues relate to the novel subwoofer system itself and to the objectives that the subwoofer is intended to solve and presented below.

1.2.1 Acoustic Non-Linearity

Through frequency sweeping and musical playback, it was noted that the response of the acoustic windshield is inconsistent across frequencies with resonance discovered at 130 Hz and subsequent harmonics. The lack of a flat response to all frequencies of excitation yield undesirable audio distortion with some tones being attenuated and others peaking significantly louder than neighbouring frequencies. Figure 1.1 below is the road test frequency response of piezoelectric acoustic windshield installed in a vehicle demonstrating the non-linear acoustic response. Speakers possessing the characteristic of equal magnitude response across the frequency band of operation are preferable to those which exhibit a frequency-dependent response such as that of the piezo-electric acoustic device. A digital compensation mechanism is required to equalize the frequency response to match it with high-fidelity subwoofer cones whose construction yield an inherently linear response.

1.2.2 Ambient Highway Noise

While much effort has been put forth to improve the passenger experience within a vehicle by attenuating highway noise through means of passive dampening and noise source isolation, the increased manufacturing cost of such vehicles limit their distribution to luxury models. In economy-class vehicles, significant noise disturbance introduced by tire rotation, engine throttle, and wind vibrations continue to reduce the quality of the driving experience. With the spectra of disturbance primarily in the low acoustic bands, it is desirable to utilize the piezoelectric speaker to perform Active Noise Cancellation (ANC) using the same digital compensation mechanism previously proposed for the acoustic linearization of the speaker to reduce the audible noise interference within the vehicle cabin.

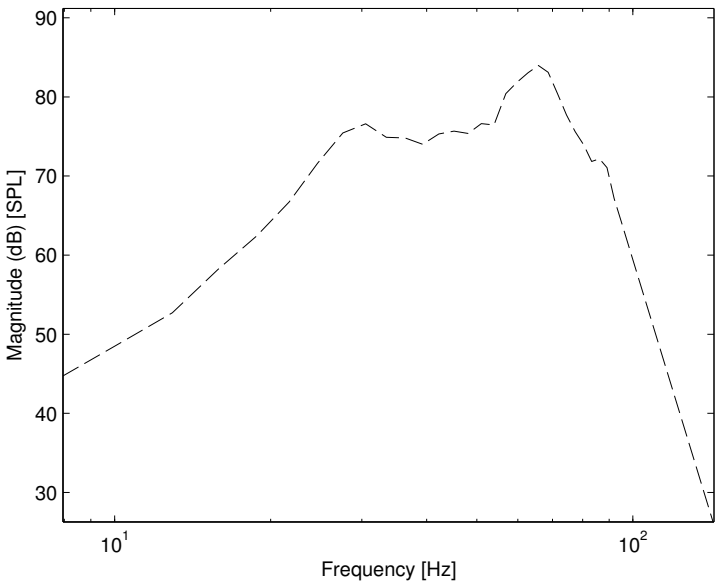

Fig. 1.1 Empirical frequency response of automotive windshield demonstrating non-linear acoustic amplification

1.2.3 Window Buffeting

Window buffeting is a phenomenon that occurs within a vehicle at highway speed operation when a single window is opened while the others remain sealed. The characteristic experience of buffeting is a high magnitude oscillatory hammering sound which results in severe discomfort for passengers. The characteristics of this noise type differ significantly from ambient noise and hence a specialized technique is sought to aid in attenuating window buffeting with the piezoelectric subwoofer. A detailed analysis of the physical phenomenon was carried out in [3] and is beyond the scope of this thesis.

1.3 Thesis Objective

The objective of this thesis is to develop a means for controlling the operation of a piezoelectric actuator to improve its acoustic performance by utilizing feedback based frequency equalization. In addition, a means for adaptive modification of the controller shall be introduced to implement active noise cancellation periodically optimized on the type of output disturbance experienced by the vehicle. A noise estimator is used to isolate the disturbance from the desired audio response within the cabin; the resulting noise is remod-

elled by stochastic subspace identification to update the controller. Using $\mathcal{H}_\infty$ optimization for disturbance rejection and loop-shaping with real-time subspace identification estimates of the output disturbance, this technique may be useful for improving the general performance of robust $\mathcal{H}_\infty$ and μ-synthesis controllers by narrowing the magnitude of uncertainty within a given system. Boulet and Duan demonstrated the necessity for controllers to trade-off performance with robustness to plant uncertainty in [4]. The fundamental performance limitation caused by unmodelled dynamics motivates a technique for narrowing the range of uncertainty, which is demonstrated in this thesis.

1.4 Thesis Roadmap

In Chapter 2, a survey of existing efforts in active noise cancellation in vehicle cabins shall be presented as well as a review of adaptive control used in $\mathcal{H}_\infty$ optimized systems. Alternative techniques for ANC will be examined which are currently being investigated for use with piezoelectrically driven buffeting suppression. Chapter 3 will introduce the experimental apparatus constructed for performing the test measurements used in this thesis. In Chapter 4, the workings and mathematics of subspace identification will be discussed and the algorithms' applicability for use with $\mathcal{H}_\infty$ synthesis is discussed. Models of the subwoofer, amplifier, and other subsystems will also be derived here. Chapter 5 will present a detailed analysis of the acoustic disturbance experienced by passengers within a moving vehicle including ambient highway noise and the window buffeting phenomenon. A noise estimator designed for performing real-time modelling of the noise characteristics will also be introduced. In Chapter 6, the controller design is presented as well as a state-machine algorithm for adaptive updates and performance optimization. Simulations of the completed system are also presented in Chapter 6 where they will be scrutinized for performance and feasibility. In Chapter 7, concluding remarks will be presented in addition to acknowledged deficits and shortfalls of the proposed control technique; future work is discussed in addition to recommendations for practical implementations.

Chapter 2

Literature Review

In this section, we begin with a literature review related to noise cancellation using both passive and active attenuation techniques. Feedforward algorithms for active noise control are explored first before surveying literature related to the feedback based ANC methods which relate to the techniques presented in this thesis. $\mathcal{H}_\infty$ control is then introduced before a review of system identification using subspace-based algorithms.

2.1 Passive Noise Cancellation

Passive noise attenuation relies on the use of the physical properties of materials to dampen the reflection or radiation of sound. Unwanted noise is attenuated through the use of such instruments as mufflers, absorbers, or diffusers. While absorbers serve to remove the sound energy in the air through characteristics of their geometry and material, diffusers provide a passive means to redirect noise energy so that it is more evenly distributed, which can be designed to reduce certain types of noise [5]. Shock absorbers are an example of passive diffusion employed in vehicles to reduce the transmission of vibrations which also quiets shocks in road noise.

As frequency decreases, the effectiveness of passive noise attenuation also decreases significantly below 500 Hz as the acoustic wavelength becomes large and the requisite thickness of absorbers becomes too large [6]. The frequency band which we seek to target resulting from highway noise and window buffeting is significantly below the range which can be feasibly attenuated by passive control as cost and physical thickness limitations constrain the problem.

2.2 Active Noise Cancellation

When passive noise attenuation alone is insufficient for achieving sufficient performance, active noise cancellation may be utilized to improve the results. A detailed tutorial of Active Noise Control is presented by Kuo and Morgan in [7] in which the benefits of active over passive noise attenuation are explored in detail. In particular, passive noise control fails to sufficiently attenuate low-frequency noise disturbances in addition to requiring large, bulky dampening devices which may not be feasible for applications in moving vehicles. In general, there exist two primary means for implementing ANC: feedforward, whereby a microphone may be used to perform a direct measurement of the disturbance and feedback, in which noise measurements may not be available. In the former scheme, the sampling microphone is typically placed in a position where direct measurement of the noise enables the production of an antiphase signal for destructive superposition. In the latter, the advantage of being able to sample the noise disturbance before it corrupts the environment is not available; subsequently, the microphone is placed where the noise attenuation is to be realized and senses both the noise and desired signal. In feedback control, the measured signal is then subtracted from the desired signal to achieve an error signal from which the antinoise signal is derived. Hybrid feedforward-feeeback controllers are also the focus of ongoing research.

The source of noise within a vehicular cabin is not unique and is, in fact, the sum result of many point sources including tire noise, wind noise, and mechanical engine noise. While each of these sources could, in theory, be sampled outside of the vehicle cabin to implement a feedforward ANC strategy, the characteristics of each such disturbance are modified as they propagate from their respective sources, external to passenger cabin where they are measured, to within the cabin itself. The acoustic transfer function of their propagation introduces uncertainty which complicates a direct actuation of the antinoise signal. Failure to directly measure the disturbance reduces the performance of feedforward ANC, however, their principle of operation will be reviewed below in addition to feedback ANC which is the focus of the remainder of this thesis.

2.2.1 Feedforward: LMS and FxLMS Algorithms

Feedforward ANC use adaptive filters whose coefficients are updated at each time-step to minimize an error signal. First introduced by Widrow and Hoff [8][9], this class of noise

attenuation algorithms typically employ one microphone to measure the noise directly and a second microphone to measure the residual error signal. With reference to Figure 2.1, the disturbance signal $d_o(n)$ enters the system at microphone A and propagates through the acoustic environment of the observer where microphone B is located. The impulse response,

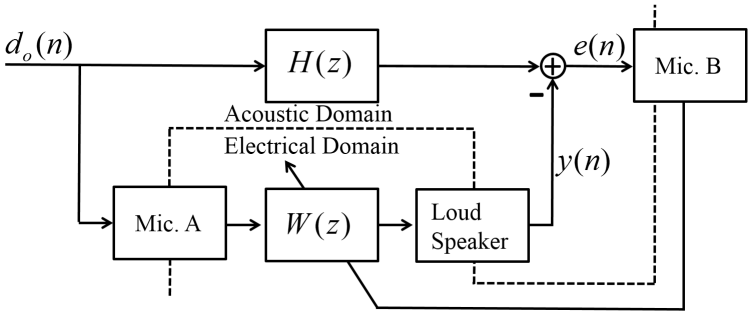

Fig. 2.1 Basic LMS Implementation.

$h(n)$ is the acoustic path between the two microphones and consists of a non-invertible time delay in addition to the characteristic dynamics of the specific environment. Letting $W(z)$ denote the Z-transform of the adaptive filter, the error signal $E(z)$ is given in [10] as:

$$E(z) = [H(z) - W(z)]D_o(z) \tag{2.1}$$

To minimize the error, we seek to obtain a filter $W(z)$ which closely matches the unknown acoustic propagation function $H(z)$, e.g.:

$$E(z) \to 0 \quad \text{as} \quad W(z) \to H(z)$$

Our objective then is to develop an adaptive $W(z)$ which, upon each update, converges on $H(z)$. Following the derivation by Boroujeny in [11], the N-dimensional weighting filter $w(n)$, whose coefficients vary in time by index n, is defined as:

$$w(n) = [w_o(n) \;\; w_1(n) \;\; \ldots \;\; w_{N-1}(n)]^T$$

The output, $y(n)$ of the speaker is hence:

$$\begin{aligned} y(n) =& w(n) * x(n) \\ =& \sum_{i=0}^{N-1} w_i(n) x(n-i) \end{aligned}$$

Taking the inverse Z-transform of (2.1) and squaring, we obtain the definition of our cost function, $C(n)$:

$$\begin{aligned} C(n) =& e^2(n) \\ =& (h(n) * d_o(n) - w(n) * d_o(n))^2 \end{aligned} \tag{2.2}$$

The basis of LMS is to use our estimate of $\hat{C}(n)$ to obtain an approximation of the gradient which is applied to improve the filter coefficients of $W(n)$ in the direction of steepest descent:

$$\begin{aligned} \nabla C(n) =& \nabla e^2(n) \\ =& \left[\frac{\partial}{\partial w_0} \quad \frac{\partial}{\partial w_1} \quad \cdots \quad \frac{\partial}{\partial w_{N-1}} \right]^T e^2(n) \end{aligned} \tag{2.3}$$

The i-th element of (2.3) may be given by,

$$\frac{\partial e^2(n)}{\partial w_i} = 2e(n) \frac{\partial e(n)}{\partial w_i} \tag{2.4}$$

Substituting (2.2) into (2.4), we may deduce the update method for the i-th filter coefficient,

$$\begin{aligned}\frac{\partial e^2(n)}{\partial w_i} =& 2e(n)\frac{\partial(h(n) * d_o(n) - w(n) * d_o(n))}{\partial w_i} \\ =& -2e(n)\frac{\partial(w(n) * d_o(n))}{\partial w_i} \\ =& -2e(n)\frac{\partial(\sum_{i=0}^{N-1} w_i(n)x(n-i))}{\partial w_i} \\ =& -2e(n)x(n-i)\end{aligned} \tag{2.5}$$

We update each filter coefficient of the vector $w(n)$ in the direction of steepest descent:

$$\begin{aligned}w_i(n+1) =& w_i(n) - \mu\nabla e^2(n) \\ =& w_i(n) + \mu 2e(n)x(n)\end{aligned} \tag{2.6}$$

where μ denotes the step-size parameter.

A practical limitation of the LMS algorithm is the secondary path of the actuated signal which represents the transfer function from the output of the controller, through the digital-to-analog conversion process, the speaker and finally the acoustic propagation to the location where the cancellation takes effect depicted by $S(z)$ in Figure 2.2.

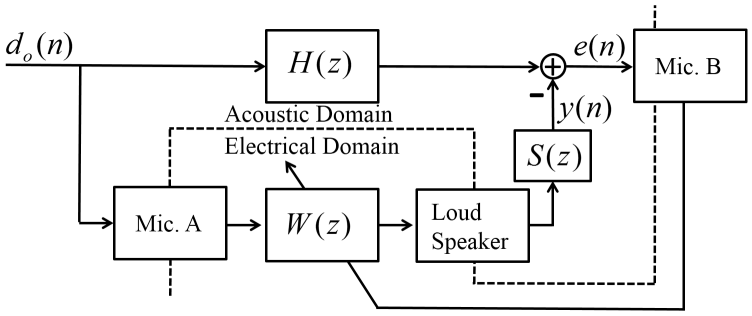

Fig. 2.2 LMS Implementation showing secondary path.

The criteria for minimal error is now:

$$E(z) \to 0 \quad \text{as} \quad W(z) \to H(z)/S(z)$$

The secondary path includes delays which prevent the direct inversion of $S(z)$ resulting

in a degradation of the stability of the algorithm. To avoid the inversion, an estimate of the secondary delay is instead used to pre-filter the incoming signal before the application of $W(z)$. Known as FxLMS, this process was developed by Widrow in [12] and improves the performance of standard LMS; a block diagram of the process is shown in 2.3.

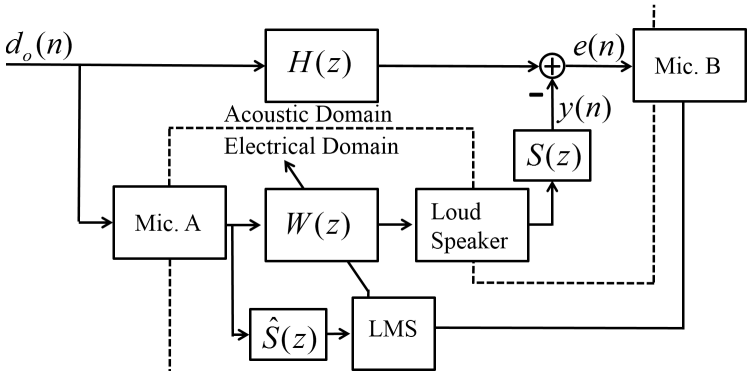

Fig. 2.3 FxLMS Implementation showing pre-filtered input $x'(n) = \hat{s}(n) * x(n)$

Here, the application of the secondary path pre-filter to input signal $x(n)$ yields a modified filtered signal $x'(n)$. The steepest descent filter update equation is then nearly identical to that of basic LMS:

$$w_i(n+1) = w_i(n) + \mu e(n) x'(n) \tag{2.7}$$

The model of the secondary path transfer function $\hat{S}(z)$ is typically estimated offline although research began in [13] for real-time path modelling and continues, such as in [14].

FxLMS algorithms have been accepted for widespread implementation primarily for their computational simplicity and generally praised performance. They have also been extended into multi-channel application as demonstrated in [15]. Efron showed in [16] a means for canceling multi-point noise sources through the weighted sum of many anti-noise actuation speakers to reduce the noise in a targeted region by correctly accounting for the superposition of all the cancelling signals. An integrated automotive ANC system using the audio system within the vehicle was demonstrated by Holmes in [17] which implements the FxLMS algorithms with good results.

Drawbacks of the FxLMS algorithm begin with the manner in which the weighting coefficients are updated. The steepest descent algorithm utilizes the instantaneous esti-

mate of the squared-error to measure the direction of the gradient. This is effectively an approximation of the second moment [18]. That is:

$$\mathrm{E}\left\{e^2(n)\right\} \approx e^2(n) \tag{2.8}$$

For correct operation and convergence to optimal filter coefficients, in the mean-squared sense, the second moment of the noise process must exist; as such, impulsive noise results in a loss of stability. An additional disadvantage of FxLMS techniques is their intrinsically feedforward requirement to measure the noise source through some isolation from region of acoustic cancellation. Additionally, it has been shown that microphone and actuation devices improve in ANC performance with increasing proximity to the noise source. This is not always feasible especially when the noise sources are not all well known prior to the implementation. Placing microphones near each noise source introduces increasing cost and complexities - issues that detract from their primarily sought characteristic of simplicity.

Engine noise has been the primary focus of ANC applications which utilize the feedforward strategy but road noise has remained out of reach due to cost and implementation limitations [19] as additional sensors are required for each noise source. In 1994, Sutton *et al.* demonstrated in [20] that to reduce road noise within a vehicle using FxLMS, it was necessary to incorporate six accelerators, two error microphones and two additional loudspeakers to implement the multi-channel FxLMS algorithm effectively.

2.2.2 Feedback

The use of feedforward techniques has dominated the research of ANC in part for their simplicity in computational implementation. With the advancement of high-performance, low-cost digital signal processors, the problem of noise attenuation has become the focus of much research in the frequency domain based feedback control systems. Recasting the problem into traditional feedback control is straightforward since disturbance rejection is a primary objective in the standard problem formulation. In Figure 2.4 below, a basic zero-input feedback control scheme is shown. The noise signal, d_o, is not measured directly as it was with feedforward control. However, its impact on the system is well-studied and quantified by the sensitivity function of which indicates the effect of output disturbance at each frequencies. The output of the system $y(s)$ is the signal perceived by the passenger,

while the reference signal $r(s)$ denotes the desired system output which may be 0 to indicate pure ANC or may contain a musical reference. The error signal $e(s)$ is the difference between the desired and measured system output. The plant, denoted by $G(s)$, contains the dynamics of the actuator (e.g. a speaker) in addition to the characteristics of the vehicular cabin between the speaker and the sensing microphone. The controller, $K(s)$ is the compensation mechanism whose dynamics are the choice of the designer.

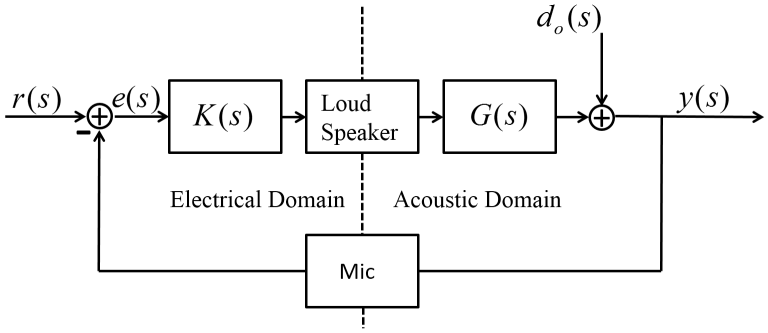

Fig. 2.4 Block diagram of feedback control implementation for disturbance rejection.

In feedback control, most of the analysis takes place in the frequency domain where insight into the characteristics and performance of the system's signals are evaluated across all frequencies.

The sensitivity function of a feedback controller describes the transfer function of many different points within the system. For our purposes, the sensitivity function represents the transfer function from the reference signal to the error, the output disturbance to the error and from the output disturbance to the output of the system. That is:

$$S(s) = \frac{1}{1 + K(s)G(s)} = T_{r\to e} = -T_{d_o\to e} = T_{d_o\to y} \tag{2.9}$$

Closely related, the complementary sensitivity function is denoted by $T(s)$ after its representation of the system's *transmission* of input to output:

$$T(s) = \frac{K(s)G(s)}{1 + K(s)G(s)} = T_{r\to y} \tag{2.10}$$

The two equations are constrained by their strict sum to unity:

$$1 = S(s) + T(s) \tag{2.11}$$

With the plant $G(s)$ fixed, the controller $K(s)$ may take on any causal form so as to shape the sensitivity and complementary sensitivity respectively. Disturbance rejection, as is the objective of ANC, is characterized by a small sensitivity function in the bandwidth of operation while the acoustic linearity of the subwoofer is best analyzed from the perspective of transmission function. With our objective to attenuate both engine and road noise within the vehicular cabin while simultaneously improving the acoustic linearity of the piezoelectric speaker, the tools of feedback control are readily applied.

It should be noted that the feedback employed in the aforementioned algorithms of Section 2.2.1 differs significantly from that in feedback *control*. In the former, the error signal is used to update the filter coefficients but is not used in the direct computation of the actuator output; instead, it is the noise reference signal on which the output is based. Feedback control, however, acts directly on the error signal to produce an anti-noise output without having access to the noise signal itself. In subsequent chapters of this thesis, a duality in the use of the error and noise signals will be demonstrated in their use in feedforward algorithms contrasted with the proposed means of adaptive optimization. The impact of true feedback in a feedforward ANC usually have a destabilizing effect should a signal from the anti-noise speaker leak back to the microphone which measures the noise [21].

An important factor to be considered in the design objective is discussed by Garcia-Bonito and Elliott in [22] where it is shown that acoustic attenuation at frequencies greater than 400 Hz is not practical since the acoustic wavelengths approach in size the targeted zones of ANC; in such an implementation, the user would experience local areas of both noise attenuation and undesirable amplification.

Hong *et al.* demonstrated in [23] an implementation of feedback control for noise attenuation in an acoustic duct using precompensated linear quadratic Gaussian synthesis which yielded a reduction in noise by 5 to 12 dB between 150 and 350 Hz. Also in the context of acoustic duct systems, PID controllers were developed and simulated in [24].

Limitations of feedback control are most notably experienced in stability margins wherein phase lag introduced by actuators in addition to sound and signal propagation delays result

in a decreased bandwidth or total loss of stability. Boonen and Sas demonstrated in [25] a technique for phase lag compensation using a Smith compensator to improve stability margins.

Feedback control for use in active noise cancellation within a vehicle was first demonstrated by Sano *et al.* in 2001 [26] wherein booming noise was successfully attenuated in the front seats of the automotive. The buffeting phenomenon, sometimes described as wind throb, was the target for attenuation in [27] which its control was demonstrated with some success. In this thesis, we demonstrate a new approach for buffeting reduction using a noise estimator to track the frequency of the buffeting more precisely thereby allowing us to implement an $\mathcal{H}_\infty$ controller matched specifically to an up-to-date noise model for improved attenuation.

2.3 $\mathcal{H}_\infty$ Control

$\mathcal{H}_\infty$ feedback control offers an appealing framework for the task of noise reduction since the objective for which the theory was derived was based on sensitivity minimization - the same objective as ANC. George Zames, a primary inventor of the theory, noted in his seminal paper [28] that a minimum phase system may have its sensitivity made arbitrarily small. Actuator limitations which may prevent the physical realization of such dramatic minimizations are readily incorporated into the design effort to guarantee optimal performance given the physical constraints.

Horowitz, in [29], presents a secondary source of limitation which prevents unbounded minimization of sensitivity: uncertainty. In addition to accommodating physical limitations of the actuation hardware, $\mathcal{H}_\infty$ methods are aptly capable of producing robust controllers for systems which possess significant degrees of unmodelled dynamics. Allen Tannenbaum presented in 1980, an algorithm for obtaining an optimal stabilizing controller for a SISO plant containing gain uncertainty [30]. While advancements in research continued to improve the performance of systems containing unmodelled dynamics, they relied on models of uncertainty which characterized the plant uncertainties by norm bounded perturbations. Information about the structure of the perturbation could not be exploited until the work of Doyle in [31] which introduced the structured singular value as a tool to incorporate such additional information to reduce the difficulty in identifying a stabilizing controller and improve the resulting performance. $\mathcal{H}_\infty$ treatment of time-varying uncertainties has

since been considered in [32] and improved upon in [33].

The toolset in $\mathcal{H}_\infty$ feedback control has been used with the objective of Active Noise Cancellation before. From the perspective of improving the feedforward algorithms, optimal filter coefficients were obtained in [34] in an alternative to FxLMS. Here, with the use of $\mathcal{H}_\infty$ optimization, an optimal filter is produced which limits the maximum energy gain of external disturbances. Feedback has also been utilized with one such notable example in 1999 by Elliott and Rafaely whom demonstrated a robust ANC system within a vehicular headrest in using techniques of H_2 and $\mathcal{H}_\infty$ control and multiplicative plant uncertainty [35].

Despite the improving tools for handling unmodelled plant dynamics, the presence of any uncertainty exists at the expense of performance in a fundamental tradeoff between performance and robustness, demonstrated by Boulet and Duan in [4]. To guarantee stability, performance is compromised with increasing plant uncertainties. In environments which possess a wide range of noise sources, each with characteristic and unknown frequency responses, a single, conservative $\mathcal{H}_\infty$ controller to optimally reduce sensitivity across all disturbances would be hence severely limited in its performance.

It is the objective of this thesis to utilize subspace identification to adaptively lessen the uncertainty of the system thereby improving global performance.

2.4 Subspace Identification and $\mathcal{H}_\infty$ Control

With the objective to narrow the band of uncertainty to achieve better performance in noise attenuation, a means for online modelling is required. Subspace identification has been growing in popularity in part for its robust numerical stability and rapid computation to produce accurate models which do not require iterative minimization [36]. Additionally, they are well suited for multiple-input multiple-output systems unlike many forms of traditional system identification which require empirical data from single variables at a time: often undesirably in open-loop environments.

The equations below show the standard discrete state-space system containing internal state variable, x_k, input u_k, output y_k and input and output noise variables w_k and v_k respectively:

$$x_{k+1} = Ax_k + Bu_k + w_k \tag{2.12}$$

$$y_k = Cx_k + Du_k + v_k \tag{2.13}$$

The task of subspace identification (SSI) is to obtain estimates of the state-space system matrices A, B, C and D directly from input-output data. The presence of noise or an excitation signal distinguish the primary classes of identification into deterministic ($w_k = v_k = 0, u_k \neq 0$), pure stochastic ($w_k \neq 0, v_k \neq 0, u_k = 0$) and combined deterministic-stochastic ($w_k \neq 0, v_k \neq 0, u_k \neq 0$). The state sequence, $x_0, x_1, \ldots, x_k$, is first estimated without any priori using an orthogonal or oblique projection of the row spaces of specifically oriented Hankel matrices which contain only input-output data. The order is then computed through inspection of the singular values before, finally, the system matrices are extracted from a solution of a least squares problem. In the presence of stochastic elements, a Kalman filter is utilized to make an optimal estimate of the state sequence before noise covariance matrices are extracted in the final step [37]. The implementation of SSI will be explained in Chapter 4, a more thorough analysis of the underlying theory can be found in [37, 38, 39].

Subspace identification of plant uncertainties remains to be well explored in literature. Stochastic identification is used to estimate system uncertainties to some extent such as in [40], where noisy measurements are filtered and estimations of parameter variance is simulated successfully. Uncertainty estimates are made in [41] using SSI in the context of operational modal analysis. Confidence intervals, which extend an analogue to uncertainty bounds in $\mathcal{H}_\infty$ design, were established to merge data from multiple sensors of multiple tests. SSI has also been used in direct combination with $\mathcal{H}_\infty$ robust control to model and control characteristically unstable active magnetic bearings in [42]; incorporating additive uncertainty was demonstrated, however, the stochastic elements of the system were not directly estimated with SSI.

For the purposes of this investigation, SSI will serve most significantly to develop an adaptive disturbance weighting function in $\mathcal{H}_\infty$ synthesis whereby an infinity norm-limited disturbance signal is modelled by stochastic subspace identification to reduce uncertainty thereby improving performance in active noise attenuation.

Chapter 3

Experimental Apparatus and Equipment Selection

Work on this thesis benefited from the generosity put forth by Auto21 and Magna International for ensuring that a working experimental apparatus was available for the data acquisition and plant analysis portions of this project. An experimental setup was designed by Magna for characterizing and evaluating the performance of Gustavsson's piezoelectric actuation apparatus for use with windshield installations. The test rig was used to evaluate the acoustic quality of the piezoelectric speaker under varying amounts of pre-loaded weight; it was shown that volume was increased with increasing compressive load on the crystals. This development led to the introduction of tensile springs on all subsequent designs whose tension could be adjusted for testing. A full-scale test system was then created of the inside front cabin of a vehicle where the actuators were mounted to a front windshield and functionality demonstrated. A vehicular installation followed using the rear windshield of a working automobile to demonstrate improving functionality; acoustic results from these tests showed good results but the presence of non-linear acoustic response remained. When work on this thesis began, automotive testing was already underway. A spare test apparatus from earlier development was donated to McGill for controls investigation.

3.1 Piezoelectric Subwoofer

The test apparatus received from Magna is shown in Figure 3.1 below. Two plates are joined into a corrugated steel assembly with one end affixed to a hinge and the other left

to rest on the piezoelectric actuator assembly. While the applied force from the hinged plate on the piezo is already substantial, experimental setups in laboratories at Magna incorporated additional fixtures for adjusting the compressive load on the actuator to further increase the force. A noted advantage of such high compressive pre-loads is that their force is significantly greater than the relative difference in wind pressure between at-rest and highway velocity conditions, this prevents drastic changes in response to vehicle speed. In vehicle installations, this pre-load is induced by tensioned springs in vehicular assemblies.

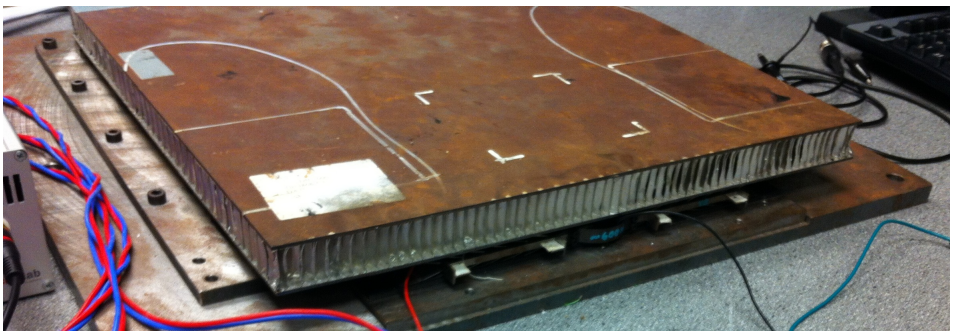

Fig. 3.1 Piezoelectric subwoofer used in laboratory tests showing Aluminium plates pivoting on single piezoelectric actuator. Plate provides pre-loaded compression to improve auditory response.

A close-up of mechanical amplification apparatus in Gustavsson's invention [1] is shown in Figure 3.2. The piezocrystal is oriented such that its oscillations occur perpendicular to the vertical vibration of the plate. A periodic signal applied by an electric potential across the piezoelectric crystal creates small, horizontal, oscillatory displacements. These reciprocating motions are then amplified and translated to the vertical plane through the pivoting motion of the rods in the invention apparatus. In this test fixture, the unhinged end of the plate is actuated upwards by the force of the piezoelectric mechanism and returned downward by its own weight. The rate at which this vertical oscillation occurs is directly indicative of the audible frequency tone produced by the device. The vibrating surface area of the plate produces compression and rarefaction pressure waves in the air which are perceived as sound by the human ear.

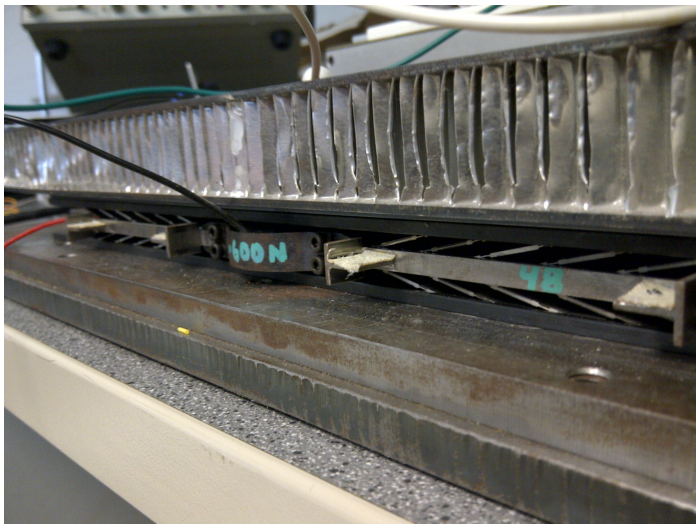

Fig. 3.2 Mechanical amplifier of piezoelectric actuator shown as described by Gustavsson's patent in [1]

3.2 Amplifier

For adequate excitation of the piezoelectric crystal, a large potential difference is necessary to transfer the control or musical reference from an electrical signal to physical vibration. To induce the smooth reciprocating motion of the windshield, characteristic of high performance speakers, smooth sine curves are required in the excitation signal. This necessitates the addition of a DC bias to adequately shape the electric field without subjecting the crystal to a damaging negative voltage. The final requirement of the amplifier is to ensure a small ripple within the bandwidth of human hearing, 15 Hz to 20,000 Hz, since any fluctuations in the signal within would be perceived as audible noise. Magna outsourced the design of the amplifier to Scienlab, a German engineering firm specializing in power electronics and electronic test equipment. Scienlab produced an Audio Class D Amplifier containing a single high-impedance, differential input channel and dual outputs capable of driving, in phase, two independent piezoelectric actuators described previously. For the purposes of this investigation, only one of the output channels was required to drive the single actuator of the test apparatus. Figure 3.3 below shows the amplifier connected to the power source and the piezoelectric amplifier.

An additional design requirement of the amplifier was that it may derive its power from standard voltage rails in vehicular installations. As such, the input may be a common

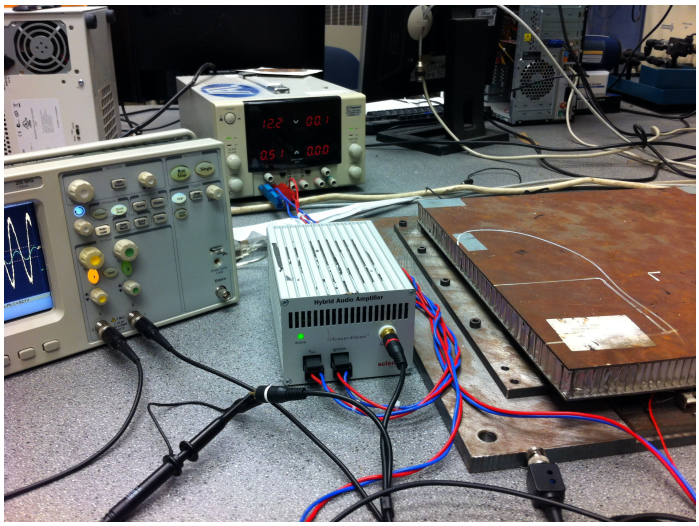

Fig. 3.3 Scienlab Hybrid audio class D amplifier and power supply connected to piezoelectric subwoofer experimental setup

DC battery power or any similar supply capable of delivering between 10V to 16V and an inrush current in excess of 7A.

An important characteristic of the amplifier from the perspective of the control design process is that it is not a direct gain element as the gain and phase delay are frequency dependent.

3.3 Microphone Apparatus

A microphone was selected as the feedback sensor used to obtain measurements of the system output. In some instances of feedforward control, accelerometers are used in place of microphones for obtaining a primary reference signal of the disturbance noise. Such implementations are advantageous when the disturbance signal is highly correlated to some underlying mechanical motion such as the RPM of the engine or tires as in [43]. With pure feedback, no direct measurement of the noise source is possible hence the most applicable sensor is a microphone.

3.3.1 Microphone

An omnidirectional measurement microphone was selected for its flat frequency response which could be treated as pure gain. An electric condenser microphone, the Apex220 has

a nearly flat response for frequencies between 20 Hz and 20 kHz with 20dB per decade roll-off beyond the cut-off frequencies. Microphone sensitivity is expressed as a single gain indicative of its output, in Volts, under the excitation of a 1 Pa sound pressure wave at 1000 Hz. Sensitivity definitions specified by US manufacturers, such as Apex, utilize a deprecated definition in which:

$$Sensitivity \Rightarrow 0 \text{ dB} = 1 \frac{\text{V}}{\mu\text{bar}} @ 1000 \text{ Hz}$$

For correct interpretation of experimental results and for accurate simulation of the system, the device sensitivity of -63dB is expressed in units of V per Pa:

$$\begin{aligned} Sensitivity = &- 63 \text{ dB} \frac{\text{V}}{\mu\text{bar}} @ 1000 \text{ Hz} \\ =&0.708 \frac{\text{mV}}{\mu\text{bar}} \\ =&7.08 \frac{\text{mV}}{\text{Pa}} \end{aligned} \tag{3.1}$$

Additional specifications of the Apex220 can be found in [44].

The phase delay, although strictly non-zero, is assumed to be such for the purposes of this investigation due to the cost limitations in the acquisition price of a phase calibration apparatus which could have yielded a more accurate model of the sensor. The phase uncertainty is also not considered in the controller design; for implementations in a vehicle, standardized microphones with calibrated phase should be utilized.

3.3.2 Phantom Power

To power the condenser microphone, the manufacturer recommends that Apex APP2 Phantom Power Supply which was acquired to ensure that the source rail would maintain the signal integrity of the measurement microphone. Phantom power supplies are capable of providing +48 VDC *to* and a signal return path *from* condenser microphones along an XLR cable. The APP2 guarantees to preserve signal integrity from 10 Hz to 25 kHz, exceeding the expected range of the ANC system. To power the phantom supply itself, an additional Apex +18 VDC supply was required.

It should be noted that during road tests for buffeting and ambient highway noise measurements, a device along the power supply path imparted a high-frequency switching noise onto the signal. Given that this phenomenon was not noted in the laboratory tests, it is hypothesized that the DC/AC inverter from the 12 V supply of the vehicle was the culprit. In future investigations, it is advisable to incorporate additional filtering in the power supply chain to improve signal integrity.

3.4 Selecting Digital Signal Processing Equipment

One of the foremost purported advantages of active noise cancellation over passive is the significant cost reduction. The hardware to implement such a control scheme must therefore be such that complexity does not drive the cost to such levels that the savings are lost.

A hardware development platform is required to serve the following purposes: perform data acquisition, perform filtering of audio signals, implement a digital controller, allow for the debugging of the system state.

Data acquisition

All of the elements in the intended control loop must be characterized so that an accurate model of their input-output behavior may be obtained. It is necessary that the development platform provide a means to record time-stamped measurements of the systems' response to excitation and a means to transfer the data to a PC for offline analysis.

Audio filtering

Some of the measurements made by the hardware module will be of signals whose magnitude is small or is corrupted by noise. Additionally, direct feedforward filters for basic signal conditioning and equalization will be of benefit to characterize the system in the testing phase.

Debugging system state

A debugger of some form is required for careful review of the testing processes and subsequent operation of the state-machine and controller implementation. The ability to pause

execution and watch variables is a good measure in best practices for ensuring deterministic behaviour of the embedded system.

Implementation of digital controller

After the design process has completed, the hardware platform must provide a means to execute a digital controller in real-time to carry out the objectives in noise attenuation and acoustic linearization. For reliable sampling frequencies, a real-time operating system with guaranteed service times or direct access to an embedded processor is ideal. Included in this requirement is the presence of multiple input and output channels which may be driven by onboard digital to analog converters (DACs) and some output filtering. The selection of a digital signal processor (DSP) capable of performing a sufficient number of cycles between samples to compute the update for the controller is a trade-off among factors such as cost, power consumption and cooling requirements. For the purposes of this investigation, it is necessary to select a processor whose capabilities exceed that which would theoretically be installed in the field for implementation in a vehicle. Additional overhead for debugging and data acquisition necessitates the selection of a development platform with a feature set that would benefit from reduction upon project completion.

In a final implementation, a custom controller board would be designed to fulfill the requirements without introducing any unused resources that may incur unnecessary cost. In the design phase, a pre-built hardware platform is selected which meets all of the aforementioned requirements in addition to providing some buffer for unforseen processing or I/O requirements.

A detailed analysis was performed in [45] which explored the selection process further. A summary of the results is shown in Table 3.1 wherein 8 potential platforms were scrutinized for their viability.

While most controller development platforms require a significant upfront capital expense, low-cost sound mixing platforms were explored as a useful alternative. Digital filtering of musical signals has become sufficiently commonplace that market prices of DSPs optimized for sound filtering have been driven down. While not typically used for data acquisition as would in the laboratory setting, music DSPs containing high frequency analog to digital converters in addition to digital to analog converters with the added benefit of built-in codecs and sampling rates optimized for audio performance. The Symphony SoundBite

Table 3.1 Potential DSP development platforms and parameters

	Type	# of inputs	# of outputs	MIPS	Estimated Price
Real-time MATLAB Simulink via Opal RT and QNX	PC/ Windows	16	2	PC Dependent	$2,680.00+
Freescale Symphony DSP Embedded System	Embedded	16	2	150-500	$1,000.00 - $1,140.00
Symphony SoundBite - Affordable Audio DSP Development Kit	Embedded	8	8	180	$150.00
Multichannel Audio Board for DA830 EVM / OMAP-L137 Starter Kit	Embedded + UNIX for development	8	8	300 for DSP + 300 for ARM9	$964.00 (option A) $1,599.00 (option B)
DSP Starter Kit (DSK) for the TMS320C6713	Embedded	3	2	1800 (1350 MFLOPS)	$450.00
TMS320C6424 Evaluation Module	Embedded	2	2	560	$515.00
TLV320AIC34 Evaluation Module (EVM) with HPA 5-6K Interface Evaluation Module to arbitrary DSP daughter card	Embedded	6	6	1800 (1350 MFLOPS)	$615.00
PCM3168A Evaluation Module DEM-DAI3168A EVM	Embedded	6	8		

platform best satisfied the criteria for implementation; included in the platform are multiple AK4556 24bit 192 kHz audio CODECs for high performance digital audio sampling and reproduction. Typically used for basic audio mixing and filtering between input channels, it was noted the onboard Freescale DSP56371 could also serve as a digital controller with a single-core clock-speed of 180MIPS.

3.5 Data Acquisition

The data acquisition was performed using a combination of a digital oscilloscope, the DSP board and a USB link to the PC. A digital low-pass filter was implemented on the DSP to perform all measurements that required the use of the microphone, which served to add gain to the audio measurements and filter out high frequency noise. Input-output measurements were taken from the respective ports of each subsystem used in the analysis to analyze their gain and phase response subject a frequency sweep in the range of 15 Hz to 900 Hz. Higher frequencies are ignored as the piezoelectric actuators are designed to operate in subwoofer bandwidth frequencies only. In some instances, a single test incorporates several transfer functions hence it is necessary to combine the results from several tests to determine the behaviour of a single element. To characterize the subwoofer, for example, the transfer function from input [V] to output [Pa] cannot be obtained in a single test. Instead, we perform multiple tests from which the speaker's transfer function may be deduced: first by characterizing the microphone, then by characterizing the DSP implementation of a LPF followed by a final test of the subwoofer cascaded with the microphone and DSP LPF. The behaviour of the piezoelectric speaker is then extracted through appropriate gain division/multiplication and phase addition/subtraction. The subsystems that were tested include:

DSP - Unity gain test

Input: Output from PC auxiliary cable
Output: Output port of DSP direct feed-through

DSP - LPF test

Input: Output from PC auxiliary cable
Output: Output port of DSP implementation after LPF to add microphone gain of x100

Amplifier

Input: Output from DSP into input of loaded AMP
Output: Output from amplifier into input of piezoelectric subwoofer

Subwoofer

Input: Output from amplifier into subwoofer
Output: Output of microphone after passing through DSP LPF with x100 gain

3.5.1 Oscilloscope

The DSP platform did not support the built in functionality of transferring large batches of data directly to the PC. While such an operation may be coded, it was deemed more efficient to utilize an available digital oscilloscope for the remainder of the data acquisition. The oscilloscope, a Welec W2000A, possesses two input channels and a 100 MHz analog bandwidth in addition to the sought characteristic of a USB interface to the PC. Figure 3.4 below shows experimental setup in operation as data acquired from a subwoofer test.

3.5.2 DSP Low-Pass Filter

In initial tests, it was found that the microphone measurements were near the noise floor and hence were corrupted with substantial high frequency noise. The increased difficulty in performing accurate measurements led to the incorporation of a digital filter to improve the testing results. A digital filter is implemented on the Freescale DSP so as to reduce the high-frequency noise and add a gain factor for 40dB to the microphone output. This filtering DSP is accounted for in all subsequent models either through self-negation when it is present in both the numerator and denominator of a transfer function data set, or, through subsequent numerical removal of its gain/phase contribution. It is noted that the former technique is preferred since it requires no additional operations which may introduce errors as is in the case with the latter.

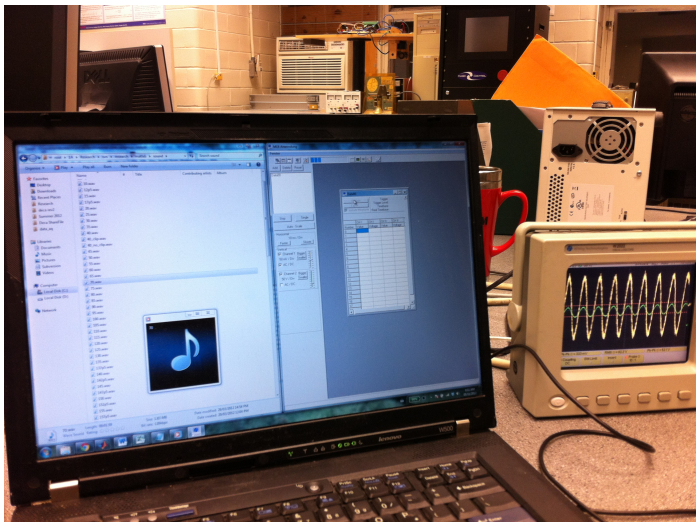

Fig. 3.4 Data acquisition experimental setup utilizing a Welec W2012A digital oscilloscope interfaced to the Freescale Symphony SoundBite audio demonstration board and W500 ThinkPad.

3.5.3 USB-Link

Information from all tests is first imported into comma-separated value (CSV) on the PC through device driver software included with the Welec oscilloscope. This process, while convenient, is subject to the delays in timing inherent to any interaction with a non real-time operating system. As a result, precisely timed measurements were not possible and so the measurements were performed on a frequency by frequency basis as opposed to impulse response or other such techniques. For accurate measurement of the zero-crossings, explained in Chapter 4 for phase extraction, the signals were oversampled typically by a factor of 50; however, the buffer size of the W200A allowed for only 3932 samples. The limiting buffer size of the oscilloscope also meant that tests are necessarily performed in small batches where it is not feasible to test more than one frequency at a time.

Subspace identification has the capacity to obtain an accurate model of a system if the excitation is sufficiently rich. However, given the brevity of the buffer, such an excitation signal may have to incorporate substantial frequency information in a compact number of samples. The unknown resonant peaks of the subwoofer, which were said to exist by Magna, made this technique of identification high-risk should a such a high-energy excitation cause damage to the piezoelectric crystal.

The CSV data is then imported into MATLAB^{TM}where the remainder of the analysis

takes place.

Chapter 4

Modelling and Subspace Identification

An accurate model of the plant is necessary for the implementation of feedback control in ANC and hence a significant portion of this project is devoted to developing techniques for obtaining a good model of the system dynamics and most importantly, for keeping that model up to date.

The plant, consisting of the subwoofer and its driving amplifier, will be used to implement a noise estimator in subsequent sections of this thesis. For this reason, it was desired that a model be obtained for these subsystems which demonstrated as little uncertainty as possible. While the nature of $\mathcal{H}_\infty$ design allows for uncertainty if it has been properly incorporated in the synthesis, we would like to focus our uncertainty metrics on the noise disturbance and not the plant itself. For this reason, we utilize deterministic subspace identification to model the plant dynamics. To carry out pure deterministic identification, we require the use of the assumption that the measurements contain no noise so that we may deduce that the output is a direct result from the input subject to the internal dynamics of the system. The empirical data from the experiments in addition to the merging procedures that were necessary to deduce the behaviour of single elements within larger, cascaded systems, necessarily introduced more noise than could reasonably be assumed zero. To account for this, we introduce pre-processing steps to filter the data before applying the tools of deterministic subspace identification. While subspace identification is a discrete-time domain algorithm which directly allows for the computation of state-space

matrices from input-output data, we shall utilize some tools from the frequency domain to simplify the synthesis of the final data set on which we may apply the SSI.

It should be noted that the techniques employed in this thesis vary in their domain of implementation. The system identification algorithms utilize theory based in the discrete-time, state space domain. The $\mathcal{H}_\infty$ synthesis theory, on the contrary, utilizes continuous-time state space models of the plant dynamics. Implementation of an $\mathcal{H}_\infty$ controller is, however, in the discrete-time domain on-board a digital signal processor. Analysis of the systems studied in this investigation are, therefore, not carried out in strictly the continuous or discrete domains since the models must be well-conditioned in both.

We assume that all elements in the plant are completely linear time-invariant (LTI) and since each sample set contains only a single frequency of excitation, we may deduce that the system's response is constant for the duration of the measurement period. From this deduction, it can then be concluded that despite all corruption effects of the stochastic noise, our objective is to identify only two variables from each sample-set: gain and phase. Our procedure is hence to develop an automated technique for accurately measuring the gain and phase of each sample batch. From this information, we then synthesize new, noise free, input-output channels on which deterministic SSI can be implemented.

To measure the two parameters, we utilize the method of zero-crossing detection to compute the time-delay between the signals. During the experimental procedure, the sampling rate of the oscilloscope is adjusted to guarantee at least ten complete waveforms in each sample-set. We therefore can perform a sufficient number of zero-crossing measurements in each set to estimate the mean zero-cross time delay.

As shown in Figure 4.1(a), a reliable means to automatically compute the phase delay is difficult given the presence of the corrupting noise. The precise timing of the zero-crossing event is not clear with the voltage spikes which speckle the data. Sources of the high-frequency noise are many including the multiple ADC/DAC conversions in the measurement procedures, the noise floor of the microphone, ambient noise in the laboratory, and the numerical and quantization errors introduced by the finite precision machinery. Additionally, most signals in the experimental results are biased above 0 V by some amount; it is therefore not a *zero*-crossing event that we seek but rather a *mean*-crossing. Low frequency noise also corrupts the signals which results in a time varying mean.

To reduce the impact of such noise, we employ a self-negating bandpass filter which was first discussed in the previous chapter.

Denoting the input measurements by x_k with a frequency domain equivalent of $X(z)$ and the output by y_k and $Y(z)$ respectively. We define the transfer function, $T(z)$ of the subsystem by:

$$T(z) = \frac{Y(z)}{X(z)} \tag{4.1}$$

With both $X(z)$ and $Y(z)$ corrupted with noise, we require a means to modify each data-set to facilitate measurement of their relationship without introducing significant errors or change to the relation. Suppose we create a high-order bandpass filter, $F_{bp}(z)$ such that all frequency content above and below the frequency of excitation is attenuated significantly:

$$\begin{aligned}\hat{X}(z) :=& F_{bp}(z)X(z)\\ \hat{Y}(z) :=& F_{bp}(z)Y(z)\end{aligned}$$

Any analysis performed on $\hat{X}$ or $\hat{Y}$ would require that we incorporate information about the filter F_{bp} to deduce information about the original signal. However, since we only require the magnitude and phase relating the signals, the application of the filter does not impact the result:

$$\begin{aligned}\frac{\hat{Y}(z)}{\hat{X}(z)} =& \frac{F_{bp}(z)Y(z)}{F_{bp}(z)X(z)}\\ =& \frac{Y(z)}{X(z)}\\ =& T(z)\end{aligned}$$

The bandpass filter design is automated by first obtaining the fast Fourier transform of the signals and obtaining the frequency of excitation by:

$$\omega_c = \arg\max_{\omega} |X(z)|_{z=e^{j\omega}} \tag{4.2}$$

Next we construct the filter with resonant frequency precisely at the frequency of excitation, ω_c. It is not required that the precise characteristics of the filter be either known nor controlled since it will be effectively negated, however, in this investigation the filter was selected to have a gain of $K = 27$ and quality factor of $Q = 1$. Here, we utilize the well-

known characteristics of a the second-order continuous time filter followed by the bilinear transform to create the desired band-pass filter F_{bp}:

$$F_{bp}(s) = \frac{K}{\frac{Q}{\omega_c}s^2 + s + Q\omega_c} = \frac{27}{\frac{1}{\omega_c}s^2 + s + \omega_c} \tag{4.3}$$

Transforming to the z-domain with the bilinear transform at the sampling frequency of the oscilloscope, we obtain a difference equation which may be used to directly filter the input and output measurements,

$$F_{bp}(z) = F_{bp}(s)\big|_{s=\frac{2}{T}\frac{z-1}{z+1}, T=\frac{1}{f_{scope}}} \tag{4.4}$$

It should be noted that although the presence of the filter is negated from impacting the final gain and phase measurements; the filter's effect is not lost since it *does* effectively remove the noise from the measurement signals which greatly improves the accuracy in measuring their relationship. The magnitude and phase of $\hat{x}$ and $\hat{y}$ are indeed altered significantly by the filter but most importantly: they are altered in an identical way.

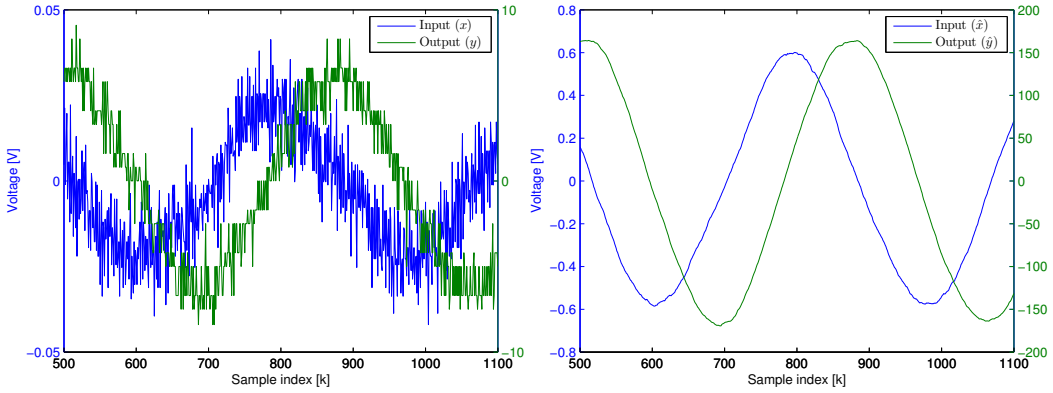

(a) (b)

Fig. 4.1 (a) Raw data measurements from experimental setup showing noise corruption of input-output, (b) Filtered data after the application of F_{bp} to input and output signals respectively.

Figure 4.1(b) shows the effect of the band-pass filter on improving the signal integrity. Information in all frequency bands is modified, however the *relative* magnitude and delay between the input and output at a single frequency is preserved. A zero-crossing detection algorithm can now be implemented.

Zero Crossing

With any DC bias removed by the band-pass filter, zero-cross detection is performed by iterating through the data and keeping track of the sign until a change has been experienced. A debounce of 30 samples is used as a final measure to filter out noise to ensure that a true zero-cross has been detected. Once the critical value is found, linear interpolation is performed to compute the best estimate of the true zero cross time. The resulting zero-cross times are then vectorized and subtracted output from input to achieve the time delays from which the mean is computed and finally multiplied by ω_c, to obtain the phase angle. Matching input and output frequencies, strengthened our assumption of the system being LTI, this was noted during the process of filter design wherein the I/O signals were transferred to the Z-domain to gauge the band-pass filter performance.

Magnitude

To determine the gain, the signals are isolated between their first and last zero-crossings to remove any bias added by non-zero incomplete periods. The root mean square is then computed for each signal and the results divided.

Figure 4.2 shows the resulting partial waveforms after processing with the bandpass filter; the zero-crossings are highlighted on the curves. Unpaired crossings, as would be indicated by the right-most $'x'$ in the figure if the complete waveform were shown, are ignored. Here, only rising edge zero-crossings are marked.

4.0.4 Input-Output synthesis

The dynamics of system given the experimental results are now contained in vectors of magnitude and phase information. The aforementioned procedure is performed in an attempt to remove as much noise as possible to effectively apply deterministic subspace identification. In a final step, it is necessary to synthesize input-output signals of pure sine waves subject to the collected data. While it seems redundant to have compressed the I/O information into two parameters of magnitude and phase only to re-expand the data into synthetic I/O streams, the process ensured that high-frequency corruptive noise would not be present for the deterministic subspace identification in a subsequent step.

Depending on the subsystem under analysis, it may be necessary to perform an additional operation on the magnitude and phase arrays before we may produce an I/O stream

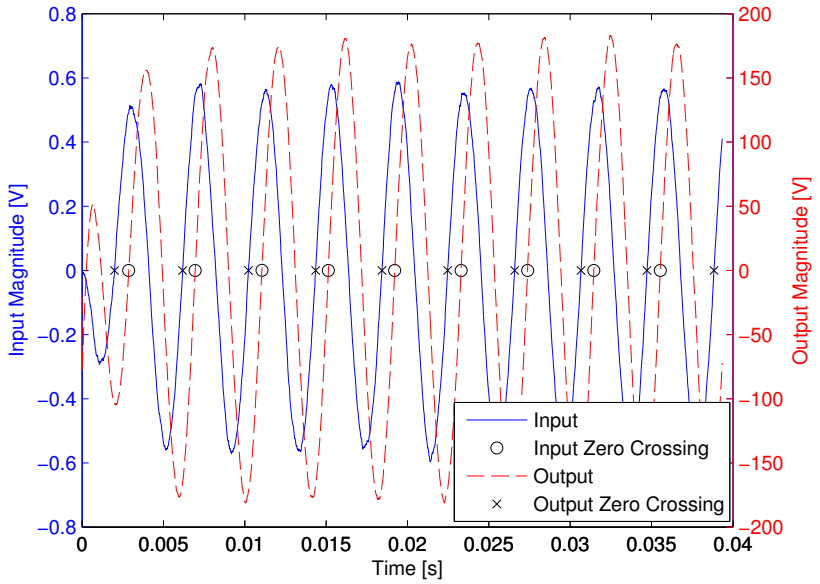

Fig. 4.2 Automated phase measurement using averaged zero crossing time delays. 245 Hz wave form shown with measured phase of -71 degrees and gain of 50 dB.

that represents the frequency response of a particular element. Let us return to the previous example of the piezoelectric actuator in which it was stated that the transfer function from input voltage [V] to output sound pressure waves [Pa] cannot be computed directly. Instead, the DSP was utilized with a high gain low pass filter so as to improve the signal integrity. Let us define the array of gain measurements of a test k such that $M^k_{A\to B}$ denotes the gain from measurement point A to B. Then the following tests were performed:

$$\begin{aligned} M^{T1}_{subwoofer\to DSP_{out}} &:= M_{mic}M_{DSP}M_{subwoofer} \\ M^{T2}_{DSP_{in}\to DSP_{out}} &:= M_{DSP} \\ M^{T3}_{mic_{in[Pa]}\to mic_{out[V]}} &:= -63 \text{ dB} \end{aligned}$$

To obtain frequency response indicative of the piezoelectric speaker from input (Volts) to output, in (Pascals), we use data from each of the three tests as follows:

$$\begin{aligned} M_{subwoofer} &= \frac{M_{mic}M_{DSP}M_{subwoofer}}{M_{mic}M_{DSP}} \\ &= \frac{M^{T1}_{subwoofer\to DSP_{out}}}{M^{T2}_{DSP_{in}\to DSP_{out}}M^{T3}_{mic_{in[Pa]}\to mic_{out[V]}}} \end{aligned}$$

where vector division and multiplication is performed element by element.

A similar procedure is used to compute the phase with the exception that time delays are additive in cascaded systems hence the phase is computed as a sum rather than a product.

The subsystems are now ready for decompression through the process of I/O synthesis. Each magnitude and phase pairing is allotted a minimum of 800 samples such that the next occurring zero-cross after 800 samples marks the beginning of the subsequent frequency; this prevents discontinuities which would introduce high frequency noise. Figure 4.3(a) shows the magnitude and phase points of the piezoelectric subwoofer from the laboratory experiments prior to the synthesis of the noise-free data. In (b) the output of the system is shown given unity gain input. After the completion of data-collection from the oscilloscope,

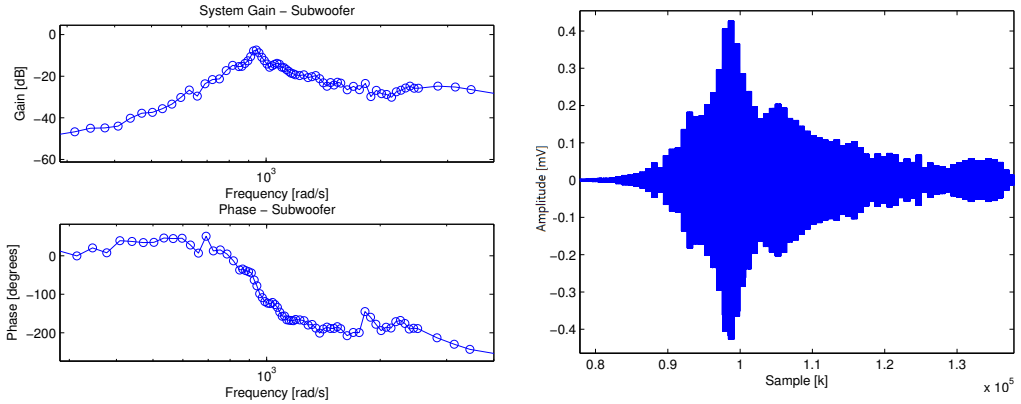

(a) (b)

Fig. 4.3 (a) Frequency response of piezoelectric subwoofer in laboratory setup after magnitude and phase extraction, (b) Synthesized I/O data used for deterministic subspace identification of piezoelectric subwoofer.

all of the algorithms discussed above are performed automatically so as to increase the efficiency with which experiments can be carried out and decrease the likelihood of human error. It should be noted that this procedure was repeated for all subsystems used in the experimental analysis.

We are now ready to perform deterministic subspace identification on the plant to obtain our state-space model.

4.0.5 Subspace Identification: Deterministic

Subspace identification, introduced in the previous section, is a method in which the system state is first derived directly from input-output data before, in a final step, the system matrices are computed. The derivation of the mathematical foundations, however briefly presented here, are largely thanks to the detailed analysis of the algorithms presented in [37, 38, 39].

We begin by first restating the general discrete representation of an LTI process:

$$\begin{aligned} x_{k+1} &= Ax_k + Bu_k + w_k \\ y_k &= Cx_k + Du_k + v_k \end{aligned}$$

Since we may now assume that the process contains zero noise, we may proceed by simplifying the model to omit w_k and v_k:

$$\begin{aligned} x_{k+1} &= Ax_k + Bu_k \\ y_k &= Cx_k + Du_k \end{aligned} \tag{4.5}$$

With knowledge of only u_k and y_k we seek to determine the order and the system matrices A, B, C and D.

In presenting the subspace identification algorithms, we follow the notation of Van Overschee and De Moor in [38] upon which most of the derivation is based.

We begin by defining two projections which are crucial in understanding the derivation of SSI: the orthogonal projection and the oblique projection.

Fig. 4.4 (a) Orthogonal projection (b) Oblique projection

The rowspace of a matrix A is projected onto the rowspace of a matrix B through the

following operation:

$$A/B = AB^T(BB^T)^{\textcircled{-1}}B$$

This operation is called the orthogonal projection and is shown geometrically for a two-dimensial system in Figure 4.4(a). The orthogonal projection utilizes the Moore-Penrose pseudoinverse [46], with shorthand $(\cdot)^{\textcircled{-1}}$.

We can use the orthogonal projection as a means for decomposing the row space the matrix, A, into the sum of two orthogonal row spaces such as:

$$A := A/B + A/B^{\perp}$$

We can also decompose A into the sum of two non-orthogonal row spaces by introducing the oblique projection. Suppose that:

$$A \in \mathbb{R}^{m\times n}, \quad B \in \mathbb{R}^{r\times n}, \quad C \in \mathbb{R}^{s\times n}$$

the oblique projection of the row space of A along the rowspace of B on the rowspace of C is defined as:

$$A/_C B := A\begin{pmatrix} C^T & B^T \end{pmatrix} \cdot \left[\begin{pmatrix} CC^T & CB^T \\ BC^T & BB^T \end{pmatrix}^{\textcircled{-1}} \right]_{s \text{ columns}}$$

We can then decompose A as follows:

$$A := A/_C B + A/_B C + A/_{C^{\perp},B^{\perp}} \begin{pmatrix} B \\ C \end{pmatrix}^{\perp}$$

It is worth noting that $B/_B C = 0$ and $C/_B C = C$.

Before the main theorem of deterministic subspace identification can be stated, we require the augmentation of (4.5) into a form that encompasses *all* of the measurement data rather than only a single sample. Let us define the state sequence matrix by a vector

which contains the progression of states sequenced horizontally as in:

$$X_i := \begin{pmatrix} x_i & x_{i+1} & \dots & x_{i+j-2} & x_{i+j-1} \end{pmatrix} \in \mathbb{R}^{n\times j}, x \in \mathbb{R}^{n\times 1}$$

The input-output data is placed into block Hankel matrices by dividing the data into *past* and *future* data sets relative to some arbitrary point within the data. The output block Hankel matrix is shown below:

$$Y_{0|2i-1} := \left(\begin{array}{ccccccc} y_0 & y_1 & y_2 & y_3 & \cdots & y_{j-2} & y_{j-1} \\ y_1 & y_2 & y_3 & y_4 & \cdots & y_{j-1} & y_j \\ y_2 & y_3 & y_4 & y_5 & \cdots & y_j & y_{j+1} \\ \cdots & \cdots & \cdots & \cdots & \cdots & \cdots & \cdots \\ y_{i-1} & y_i & y_{i+1} & y_{i+2} & \cdots & y_{i+j-1} & y_{i+j-2} \\ \hline y_i & y_{i+1} & y_{i+2} & y_{i+3} & \cdots & y_{i+j} & y_{i+j-1} \\ y_{i+1} & y_{i+2} & y_{i+3} & y_{i+4} & \cdots & y_{i+j-1} & y_{i+j} \\ y_{i+2} & y_{i+3} & y_{i+4} & y_{i+5} & \cdots & y_{i+j} & y_{i+j+1} \\ \cdots & \cdots & \cdots & \cdots & \cdots & \cdots & \cdots \\ y_{2i-1} & y_{2i} & y_{2i+1} & y_{2i+2} & \cdots & y_{2i+j-1} & y_{2i+j-2} \end{array}\right) \in \mathbb{R}^{2i\times j}$$

The element y_i is referred to as the *present* and hence when it occurs in the first column, we use its corresponding row position to divide the Hankel matrix into two block matrices where the upper block is defined as the *past* since the first column begins with y_0 and increased to y_i. The lower block is defined as the *future* since it possesses all of the outputs from the present i to the final measurement. This concept is expressed in shorthand notation by:

$$Y_{0|2i-1} := \left(\frac{Y_p}{Y_f}\right) = \left(\frac{Y_{0|i-1}}{Y_{i|2i-1}}\right)$$

We can shift the division point a below the present element which results in the advancement:

$$Y_{0|2i-1} := \left(\frac{Y_p^+}{Y_f^-}\right) = \left(\frac{Y_{0|i}}{Y_{i+1|2i-1}}\right)$$

The size of the block Hankel matrix $Y_{0|2i-1}$ is $\mathbb{R}^{2i\times j}$; the lengths i and j are arbitrary but

are typically adjusted so as to ensure that every data sample is incorporated in each row and there are at least as many rows as the maximum order of the system. An identically structured block Hankel matrix $U_{0|2i-1}$ is created which incorporates all of the input measurements. Similarly, we augment further the I/O data by placing it into a matrix $W_{0|i-1}$ (after Willems [47]):

$$\begin{aligned} W_p :=& W_{0|2i-1} \\ =& \begin{pmatrix} U_p \\ Y_p \end{pmatrix} \end{aligned}$$

We may introduce a single process equation to define our state space that includes all of the system data:

$$\begin{aligned} X_f =& A^i X_p + \Delta_i U_p \\ Y_p =& \Gamma_i X_p + H_i U_p \\ Y_f =& \Gamma_i X_f + H_i U_f \end{aligned}$$

where Γ_i is analogous to the extended controllability matrix, Δ_i to the extended observability matrix and H_i is a block triangular Toeplitz matrix. Letting l denote the number of outputs, the matrices are shown below:

$$\Gamma_i = \begin{pmatrix} C \\ CA \\ CA^2 \\ \dots \\ CA^{i-1} \end{pmatrix} \in \mathbb{R}^{li \times n}$$

$$H_i = \begin{pmatrix} D & 0 & 0 & \dots & 0 \\ CB & D & 0 & \dots & 0 \\ CAB & CB & D & \dots & 0 \\ \dots & \dots & \dots & \dots & \dots \\ CA^{i-2}B & CA^{i-3}B & CA^{i-4}B & \dots & D \end{pmatrix} \in \mathbb{R}^{li \times mi}$$

$$\Delta_i = \begin{pmatrix} A^{i-1} & A^{i-2}B & \dots & AB & B \end{pmatrix} \in \mathbb{R}^{n \times mi}$$

The deterministic subspace identification begins by first performing an oblique projection of the rowspace of Y_f along the rowspace of W_p on the rowspace of U_f. Under the assumption that intersecting rowspaces between U_f and X_p is null, it can be shown that the result from this projection is in fact, equivalent to the product of the extended observability matrix and the state sequence:

$$\Gamma_i X_f = Y_f /_{U_f} W_p \tag{4.6}$$

The proof has been omitted from this thesis but can be found in [38]. Two user defined weighting matrices $W_1 \in \mathbb{R}^{li \times li}$ and $W_2 \in \mathbb{R}^{j \times j}$ subject to the requirement that W_1 is full rank and $rank(W_p) = rank(W_p W_2)$, are defined which control the state space basis of the final model. Let us assume that $W_1 = I$ and $W_2 = U_f^{\perp T}(U_f^{\perp} U_f^{\perp T})^{\textcircled{-1}} U_f^{\perp}$. We now perform a singular value decomposition on the result from (4.6):

$$\begin{aligned} W_1(\Gamma_i X_f)W_2 &= \begin{pmatrix} U_1 & U_2 \end{pmatrix} \begin{pmatrix} S_1 & 0 \\ 0 & 0 \end{pmatrix} \begin{pmatrix} V_1^T \\ V_2^T \end{pmatrix} \\ &= U_1 S_1 V_1^T \end{aligned} \tag{4.7}$$

We may infer the order n of the system by inspecting the number of eigenvalues in S_1 different from zero. The extended observability matrix may now be computed directly from the results in (4.7):

$$\begin{aligned} \Gamma_i &= W_1^{-1} U_1 S_1^{1/2} \\ &= U_1 S_1^{1/2} \end{aligned} \tag{4.8}$$

For simplicity, a similarity transform was omitted from (4.8) but may be included to improve the efficiency with which part of the state-sequence is extracted. With knowledge of the extended observability matrix, we may now obtain the state-sequence from (4.6):

$$\begin{aligned} X_f &= (\Gamma_i)^{\textcircled{-1}} \Gamma_i X_f \\ &= X_f \end{aligned} \tag{4.9}$$

Proof of (4.9) is non-trivial given that $(\Gamma_i)^{\textcircled{-1}}$ is not a general inverse, verification of this result can be found in [38].

Recalling that the state space model utilizes the system matrices to relate the previous (or *past*) state and input to the next (or *future*) state, the reason for structuring the block Hankel matrices as we did is now clear. We have computed the state sequence X_i as X_f, hence we still need to determine the state sequence one step into the future before the system matrices are readily available. To this end, we modify the oblique projection performed in (4.6) as follows:

$$\Gamma_{i-1}X_{i+1} = Y_f^{-1}/_{U_f^{-1}}W_p^{(+)} \tag{4.10}$$

Our computation of Γ_{i-1} is simplified from the previous method since it has a direct relationship to Γ_i, that is:

$$\Gamma_{i-1} = \Gamma_i[\text{with the last } l \text{ rows removed}] \tag{4.11}$$

As before, we compute X_{i+1} by applying the right-inverse of Γ_{i-1} to the oblique projection in (4.10):

$$\begin{aligned} X_{i+1} &= (\Gamma_{i-1})^{\textcircled{-1}}\Gamma_{i-1}X_{i+1} \\ &= X_{i+1} \end{aligned} \tag{4.12}$$

We have now obtained the full state sequence from our data-set of input-output measurements. We determine the system matrices A, B, C, and D by framing the problem as follows:

$$\begin{pmatrix} X_{i+1} \\ Y_{i|i} \end{pmatrix} = \begin{pmatrix} A & B \\ C & D \end{pmatrix} \begin{pmatrix} X_i \\ U_{i|i} \end{pmatrix} \tag{4.13}$$

This linear equation can be solved directly since, in theory, having contained no noise, the states are defined completely and the system is consistent.

4.1 Implementation of deterministic subspace identification

With the empirical measurements of the I/O behaviour of the subsystems obtained through the aforementioned techniques in noise filtering, we now proceed to implement the algo-

rithms behind the deterministic subspace identification. Implementation of the subspace identification algorithms is carried out using the N4SID algorithms published by Van Overschee and De Moor in the release of [38]. Given that the models of the plant will be incorporated in $\mathcal{H}_\infty$ synthesis to design our controller, the resulting discrete-time state space models are transferred to the continuous time domain using the Bilinear transform. The results are shown in Figure 4.5 which demonstrates the performance of the algorithm in modelling the piezoelectric subwoofer.

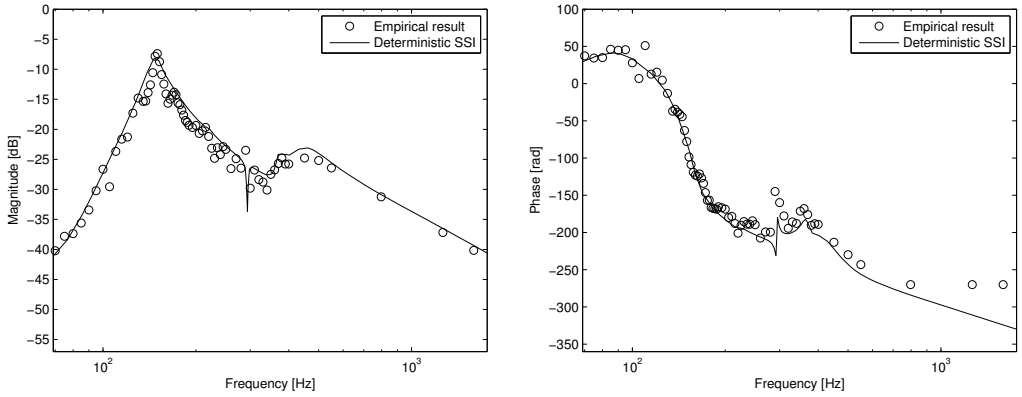

(a) (b)

Fig. 4.5 Performance of deterministic subspace identification on empirical data synthesized by intensive filtering using frequency-by-frequency band pass filters preparing for use in continuous-time $\mathcal{H}_\infty$ synthesis, (a) magnitude, (b) phase.

It is clear that while the identification method performs well in obtaining a state model which matches the empirical data, there are many limitations in using a strictly *deterministic* algorithm. Despite that we employed the filters and techniques to remove the noise from the system, it is clear that we would benefit from more reliable method of phase measurement. Amplitude measurements progress with frequency in a relatively smooth manner but the phase measurements are discontinuous. These errors introduce sharp jumps in the phase which are likely artefacts in the zero crossing method and not indicative of the behaviour of the true system. The cascading effect of such phase errors on a deterministic modelling algorithm is that the SSI will force the model to include all phase discontinuities resulting unnecessary complexity. Models derived from first principles can be advantageous since they allow for a direct physical interpretation of each pole and zero in the system. On the contrary, with fully automated modelling, we may lose sight of how to physically inter-

pret the model. Figure 4.6 shows the pole-zero map depicting the deterministic subwoofer model. Through the insight of Dr. Benoit Boulet, McGill, it is believed that most of the ORHP pole-zero pairs are likely a direct consequence of the deterministic SSI algorithm attempting to match phase discontinuities.

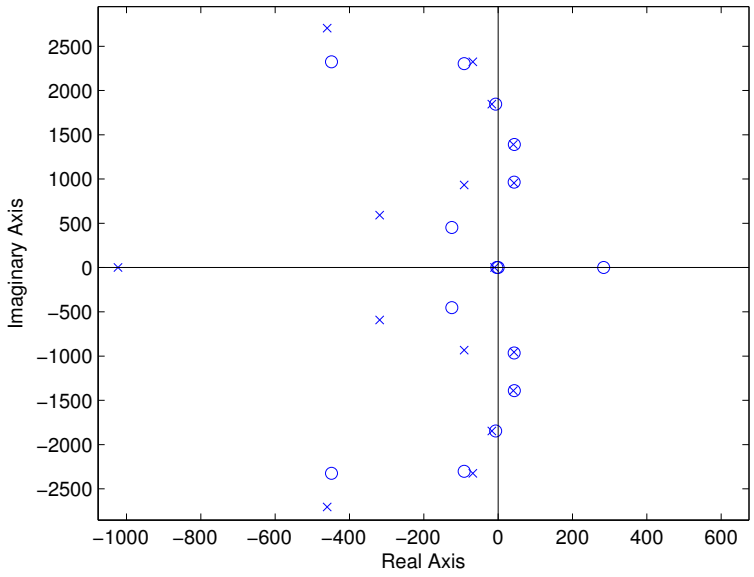

Fig. 4.6 Pole-Zero map of subwoofer system, prior to performing pole-zero cancellation of erroneous non-minimum phase zeros and unstable poles.

The techniques of $\mathcal{H}_\infty$ control are capable of handling both non-minimum phase zeros and unstable poles, however, there exist many fundamental limitations associated with the presence of either. This is especially true if we are constrained to a physical implementations where actuators have saturation limits. In initial attempts of $\mathcal{H}_\infty$ synthesis, the models developed above were used directly without any further conditioning. Artefacts introduced by the modelling techniques prevented convergence of the controller synthesis to the extent that feasible results could not be generated. It will be reasoned below that these artefacts are not actually present in the physical system and hence with discretion, we seek to minimize their impact thereby enabling the synthesis of $\mathcal{H}_\infty$ controllers. We now proceed to remove these elements in such a way that trades off the integrity of the model with simplification of controller design.

Since the models of both the amplifier and the piezoelectric speakers are known to be stable through qualitative observation, we can reasonably assume that the cancellation of erroneous phase matching NMP zeros with unstable poles can be carried out safely. The

close proximity of the poles-zero pairs in the ORHP in Figure 4.6 suggests that their removal will have only a minor impact on the phase. This was indeed found to be the case. No additional unstable poles were erroneously introduced into the system besides those that resulted from the phase artefacts.

In general, high frequency unstable poles and low frequency non-minimum phase zeros are most detrimental to the system behaviour. After experimentation with different techniques, it was found the best case model was obtained by dealing with low and high frequency non-minimum phase zeros differently. We acknowledge that our objective to remove their presence results in a less realistic model given that any acoustic cavity contains non-minimum phase zeros which are governed by the speed of sound.

The high frequency non-minimum phase zeros are removed from the ORHP by translating them into poles in the OLHP. This has the effect of preserving their phase perfectly while introducing error to the gain. Low frequency non-minimum phase zeros are translated into the OLHP by direct reflection; this preserves their magnitude perfectly but introduces phase error.

We attempt to recover some of the realism, lost as a result of our artefact removal, by utilizing lead-lag compensation to make up for the phase and gain errors that have been introduced. Again, we are faced with a trade-off by adding the compensation filters which increase the system order. The design process used to create the lead-lag filter was that of iteration by varying the filter parameters until a satisfactory trade-off between model accuracy and controller synthesis feasibility is obtained. Depending on the artefact removal technique of either translating ORHP zeros into OLHP poles, which preserved phase, or reflection of low-frequency ORHP zeros into OLHP zeros, which preserved gain; the requirements of the lead-lag filter differed. Varying the location of the pole and zero in the filter had the effect of improving *either* the accuracy of the magnitude or the phase while reducing the accuracy of the other, hence a trade-off between the conflicting effects was required. It was found that the lead-lag compensator in (4.14), performed best in yielding a model for the subwoofer which showed a good balance between gain and phase error relative to the uncompensated model. A lead-lag compensator of similar form is found for the amplifier.

$$Q(s) = \frac{2.0408 \times 10^{-7}(s+4444)^2(s+1000)(s+70)^2}{(s+400)^2(s+90)} \tag{4.14}$$

Figure 4.7 shows the effect of each modification step on the model. The original model

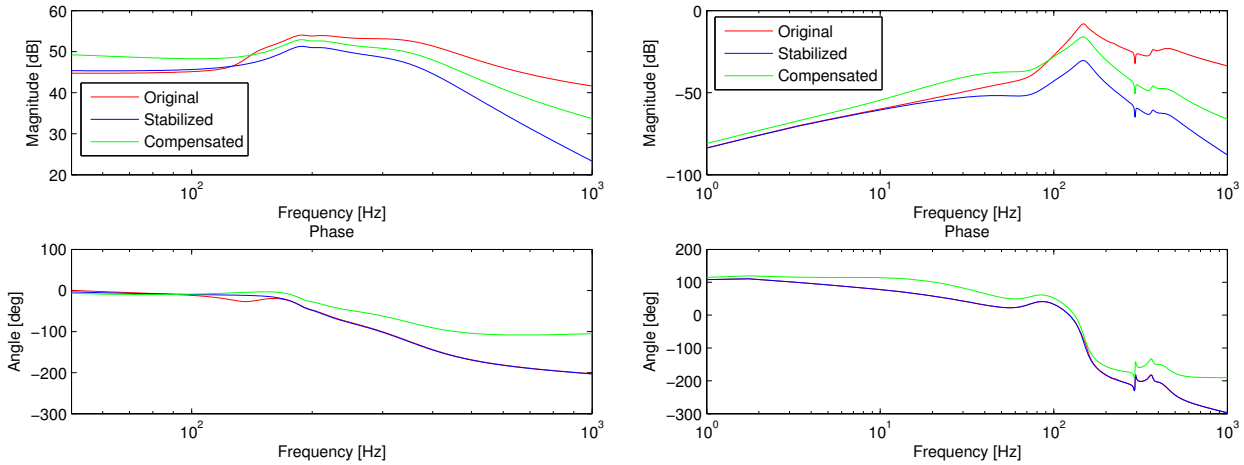

Fig. 4.7 Deterministic subspace identification introduces NMP zero and unstable pole artefacts; performance improved by cancellation improved by cancellation, reflection and inversion. Compensated with lead-lag. (a)Amplifier model (b) Piezoelectric speaker model

yielded from the subspace identification most accurately reflects the empirical data, notwithstanding errors introduced by the zero cross error, hence all subsequent compensations strive to approach the original model. Magnitude is most detrimentally impacted by the NMP zero transformations while phase remains intact. The lead-lag compensation improves the magnitude of the models to more closely match the originals at the expense of causing phase skew. The lead-lag compensators were designed to try to ensure that most phase skew was outside of the system bandwidth at frequencies greater than 200 Hz.

4.2 Model Scaling

The last step in establishing our models is to ensure that they are adequately scaled relative the noise dynamics. It was hypothesized that the resonant peaks in the piezoelectric apparatus setup in the lab would differ significantly from the model in the car. While the piezoelectric mechanism itself has characteristic modes, it is expected that most modes in the response are caused by the dynamics of the metallic plate which produces the actual pressure waves in the air through excitation by the piezo. Similarly in a vehicular

installation, the physical properties of the windshield and the fact that it is driven by two piezoelectric actuators (rather than only one as in the laboratory apparatus) are expected to result is significantly different response curve from tests in the lab. Without access to detailed vehicular test measurements, we have access to only a few test results from decommissioned prototypes; we cannot perform direct measurements on the system and hence we opt not to base our simulations on the road tests but rather to use their results to guide our approach in scaling.

Figure 4.8 shows the output of the piezoelectric speaker with excitation by a sine wave

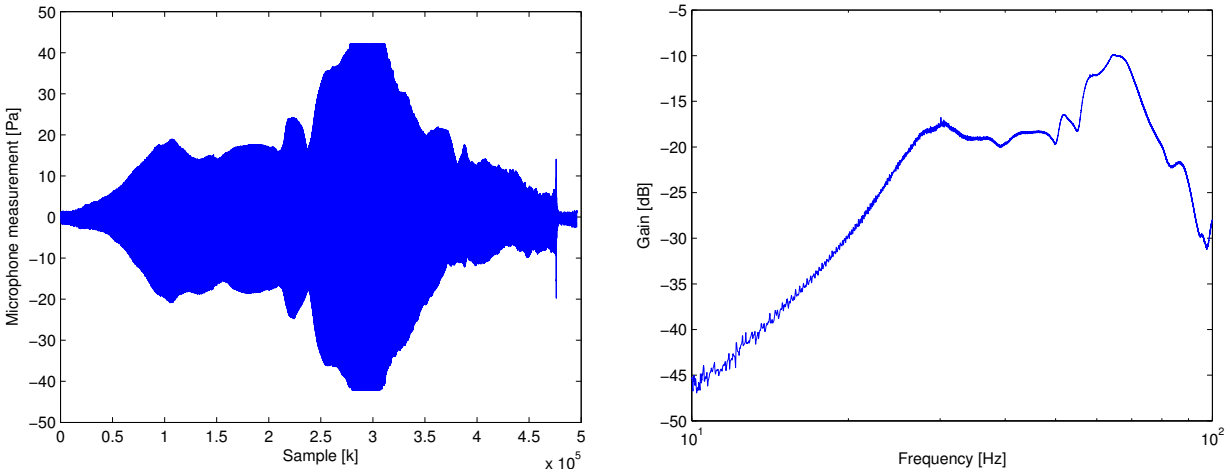

(a) (b)

Fig. 4.8 Vehicular installation of piezoelectric speaker (a) system output given sine sweep of excitation, (b) frequency response speaker output

frequency sweep in (a) and the corresponding frequency response in (b). Compared to the response of the speaker in Figure 4.5 which has most of the spectral energy concentrated above 200 Hz, empirical tests indicate that a vehicular installation of the piezoelectric system contains most of its spectral energy around 100 Hz. This discrepancy will have an impact on our controller's ability to perform noise attenuation given that it will be modelled on the laboratory response curves in Figure 4.5. The buffeting harmonics contain a fundamental mode at approximately 17 Hz, hence the system whose spectral energy is focused closer to that range (e.g. the vehicular installation) will perform better in active noise control. Our simulations then will be less indicative of real-world performance given that the spectral energy of the noise is outside that of the laboratory speaker's range.

To compensate for this discrepancy, we employ frequency scaling on the noise to shift

it into the same position in the spectra of the laboratory as the empirical noise is to the vehicular. For accurate scaling we must incorporate a model of the amplifier that was used in the vehicle. Without access to the device itself, we deduce its dynamics by dividing two frequency response curves of speaker results in the same manner that was carried out in our laboratory tests. The two tests that were combined for the amplifier behaviour deduction differed in their measured variables and their frequency sweep range. In the first test,

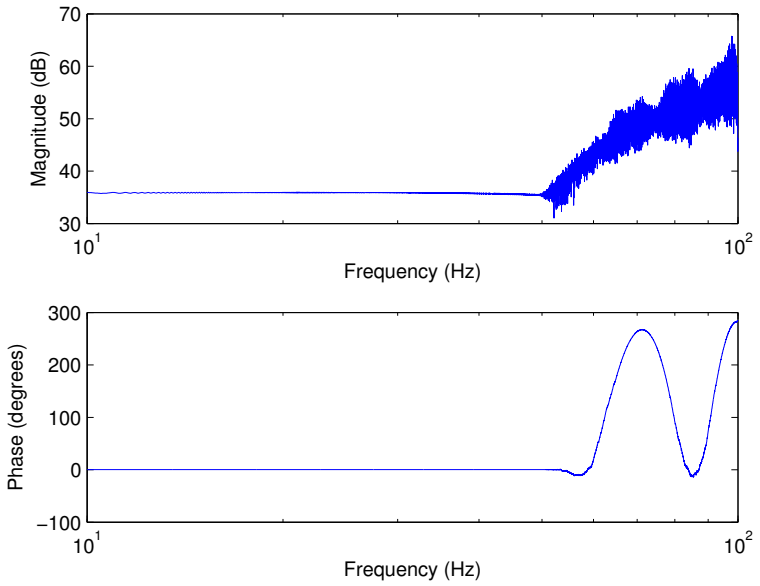

Fig. 4.9 Computed frequency response of automobile acoustic amplifier for 0 to 50 Hz showing fixed gain and phase in frequency band of interest.

measurements are present which contain data of the excitation signal streaming from the PC and of the microphone output. In the second test, measurements are present from the output of the amplifier and the microphone output. The lack of identical test conditions in the frequency sweep range complicate our ability to make an accurate inference about the amplifier's behaviour but the projected frequency response division is shown in Figure 4.9. While a more direct test method would necessarily be required to synthesize a controller to use in the vehicle, the results from our deduction are sufficient to enable an estimation of how the frequencies should be scaled.

The noise which we seek to attenuate was measured in empirical tests by the method discussed later in Section 5.1. While the techniques of stochastic system identification, presented in Section 5.2 were still being developed, the noise was quickly modelled as a

cascade of second order systems using the method presented by Marie-Pierre Jolicoeur in [48]. Once the noise was modelled, we approximate the central frequency by frequency weighting the spectral energy over the range of the sampling frequency as shown in (4.15). The result, is an estimate on central frequency of the spectrum; its value is not crucial since we are more concerned on the relative difference of ω_{av} between the noise signals and their respective piezoelectric speaker:

$$\omega_{av} \approx \frac{1}{P} \sum_{\omega=0}^{\omega_s/2} |X(j\omega)|^2 \omega \tag{4.15}$$

where P is the spectral energy of the response.

Table 4.1 Scaling of lab model to vehicular model

Model	$\approx$ Spectral E (P)	ω_{av} [Hz]
Piezo speaker (car)	0.32	119
Ambient noise (car)	0.007	65
Buffeting noise (car)	5.58	113
Piezo speaker (lab)	1.09	382
Ambient noise (lab)	0.02	208
Buffeting noise (lab)	13.8	375

Our aim is to create a shifted model of the noise whose relative position of ω_{av} compared to that of the laboratory apparatus matches that of the vehicular installation of the speaker. The results of this process are summarized by Table 4.1. By adjusting the fundamental frequency of the synthetic noise models to be used in the lab, we shift their average frequency so that they are scaled appropriately to the laboratory speaker. We adjust their spectral power in a similar way. Figure 4.10 shows the resulting magnitude response of vehicular models and those used for the laboratory system. It is clear that synthesized noise model resembles its relative position in the frequency band compared to that of the speaker. We use this model to obtain synthetic noise measurements on which we can perform stochastic subspace identification discussed section 5.2.

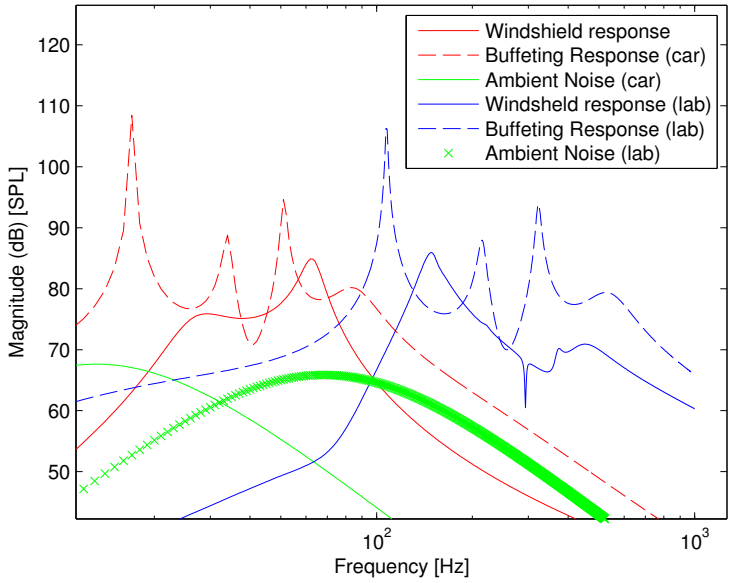

Fig. 4.10 Comparison of Models between Windshield and Full Window Buffeting Noise with Lab Model Replica and Scaled Noise

Chapter 5

Noise Estimation

5.1 Acquisition of empirical noise data

In the implementation of feedback control, direct measurement of the noise source is not performed and rather we employ knowledge of the closed-loop sensitivity function to achieve broadband noise attenuation. However, it remains a crucial point in the design stage to obtain a good model of the noise disturbance so that it may be analyzed to optimize the controller.

A 2004 Toyota Matrix is used as the test vehicle to measure the noise disturbances which we week to attenuate. The vehicle is fitted with the Apex220 microphone with its phantom power driven by an alternator connected to the standard +12 V supply within the automotive. The microphone is affixed to the approximate location of the front passenger's head. The output of the microphone is connected to a laptop to record the data. Road tests are performed in 5 km/h increments at 80 km/h and above. First, the ambient highway noise is measured by ensuring that all windows are sealed and performing measurements of the environment within the cabin without the addition of any musical reference signal. The ambient highway noise is the result of a superposition of many independent noise sources such as the tire noise, wind noise, engine noise and external traffic noise.

In subsequent tests, the buffeting phenomenon is measured by opening a single window by a sufficient amount to induce the characteristic hammering noise. The test is repeated for each window at increasing speeds to a maximum of 100 km/h. Figure 5.1 (a) shows the buffeting phenomenon recorded at a driving speed of 100 km/h; we can see the presence of the hammering tone at around 17.1 Hz its harmonics with decreasing magnitude. Figure

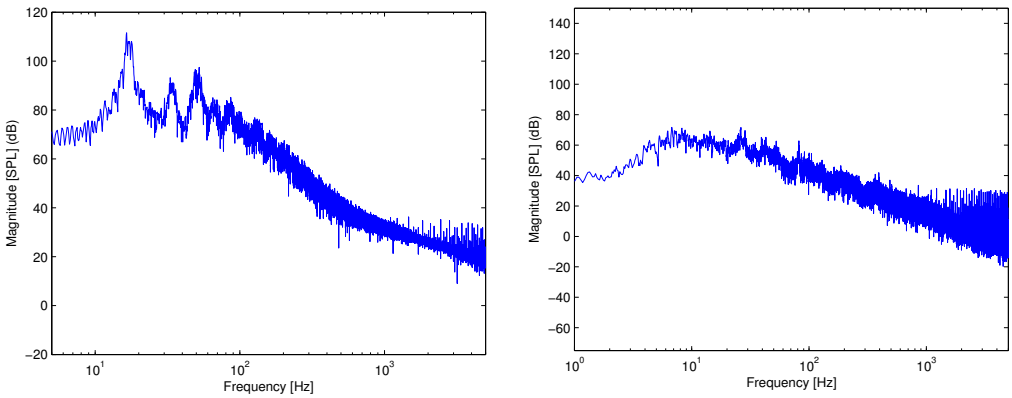

(a) (b)

Fig. 5.1 Noise measurements performed within the passenger cabin of a 2004 Toyota Matrix (a) Window buffeting recorded at 100 km/h with rear right window open, (b) Ambient highway noise recorded at 100 km/h with all windows closed.

5.1 (b) shows the noise measurements within the vehicle with all windows closed driving at 100 km/h, this is referred to at the ambient highway noise. Both tests show results plotted in units of sound pressure level (SPL) which relate the noise in Pascals as a gain from the minimum threshold of human hearing.

5.2 Subspace Identification: Stochastic

In purely stochastic subspace identification, the process input is said to be zero and the source of excitation is strictly from an external, unmeasured noise source. In $\mathcal{H}_\infty$ synthesis, we incorporate the output disturbance by directly augmenting the plant with a weighting function which we then use to enforce a physical bound on the particular $\mathcal{H}_\infty$-norm. This norm directly reflects the impact of the noise disturbance on the system output (or equivalently, on the error). This process will be explained in detail in the next chapter, suffice it to say that an accurate model of the stochastic noise disturbance is the objective of this chapter. Using the tools of stochastic subspace identification, we seek to incorporate an adaptive identification mechanism for characterizing the noise in the vehicular cabin.

We begin by restating the system process in its entirety before we proceed to identify

which special case we employ for this modelling method:

$$\begin{aligned} x_{k+1} =& Ax_k + Bu_k + w_k \\ y_k =& Cx_k + Du_k + v_k \end{aligned}$$

Previously, we made the assumption that the system was operating completely deterministically; we utilized input measurements u_k and the output measurements y_k to completely characterize the dynamics of the system model. In the stochastic model, we now assume the input noise w_k and output noise v_k to be strictly non-zero but set the input u_k to zero:

$$\begin{aligned} x_{k+1} =& Ax_k + w_k \\ y_k =& Cx_k + v_k \end{aligned}$$

Contrary to the previous method, we now have access to only a single measurement vector y_k. Our task is similar to that which was carried out previously: we seek first to identify the order of the system. Unlike the deterministic case where we could deduce exact state values, in stochastic identification we obtain optimal estimates of the state sequence instead. We then obtain the system matrices A and C from the state sequence estimate before finally making estimates of several noise statistics of the system.

To obtain estimates of the state sequence, we begin by first computing orthogonal projections on augmented block Hankel matrices of the output measurements y_k. To maintain a grasp in the physical domain, the signal y_k can be interpreted as either our direct measurement of the noise in the case of experimentation, or, as an estimate of the noise during real-time operation. As before, we acknowledge that the notation and procedure of the subspace identification algorithms is based on the work by Van Overschee and De Moor in [38]. Let us perform the orthogonal projection in an alternative method to that which relied on the use of the Moore-Penrose inverse used previously. Here, we perform an LQ decomposition of $Y_{0|2i-1}$ from which we can partition to extract the appropriate projections as shown in [37]:

$$\begin{aligned} \begin{pmatrix} Y_{0|i-1} \\ Y_{i|i} \\ Y_{i+1|2i-1} \end{pmatrix} =& \begin{pmatrix} L_{11} & 0 & 0 \\ L_{21} & L_{22} & 0 \\ L_{31}^{(l(i-1)\times li)} & L_{32} & L_{33} \end{pmatrix} \begin{pmatrix} Q_1^T \\ Q_2^T \\ Q_3^T \end{pmatrix} \\ =& LQ \end{aligned} \tag{5.1}$$

$$
\begin{aligned}
L &= \begin{pmatrix} li \times li & 0 & 0 \\ l \times li & l \times l & 0 \\ l(i-1) \times li & l(i-1) \times l & l(i-1) \times l(i-1) \end{pmatrix} \in \mathbb{R}^{2li \times 2li} \\
Q &= \begin{pmatrix} li \times j \\ l \times j \\ l(i-1) \times j \end{pmatrix} \in \mathbb{R}^{2li \times j}
\end{aligned} \tag{5.2}
$$

First we project the rowspace of Y_f onto the rowspace of Y_p as follows:

$$
Y_f / Y_p = \begin{pmatrix} L_{21} \\ L_{31} \end{pmatrix} Q_1^T \tag{5.3}
$$

It can be shown that the projection in (5.3) is equivalent to the product of the observability matrix Γ_i and the matrix $\hat{X}_i$ which contains estimate of the state sequence. Next, we perform the weighted singular value decomposition as in [37]. Again, we select arbitrary $W_1 \in \mathbb{R}^{li \times li}$ and $W_2 \in \mathbb{R}^{j \times j}$ subject to the conditions that W_1 is full rank and W_2 satisfies $rank(Y_p W_2) = rank(Y_p)$:

$$
\begin{aligned}
W_1(Y_f/Y_p)W_2 =& W_1(\Gamma_i \hat{X}_i)W_2 \\
=& \begin{pmatrix} U_1 & U_2 \end{pmatrix} \begin{pmatrix} S_1 & 0 \\ 0 & 0 \end{pmatrix} \begin{pmatrix} V_1^T \\ V_2^T \end{pmatrix} \\
=& U_1 S_1 V_1^T
\end{aligned} \tag{5.4}
$$

We may extract the system order from the number of non-zero eigenvalues in (5.4). We repeat the orthogonal projection, this time with Y_f^{-1} projected onto the rowspace of Y_p^+ to obtain the product of the observability matrix Γ_{i-1} and state sequence estimate advanced one-step forward in time:

$$
\Gamma_{i-1} \hat{X_{i+1}} = Y_f^{-1} / Y_p^+ \tag{5.5}
$$

We determine Γ_i from the results in (5.4) as follows:

$$
\begin{aligned}
\Gamma_i =& W_1^{-1} U_1 S_1^{1/2}, \quad \text{letting } W_1 \text{ be the Identity matrix, we have} \\
=& U_1 S_1^{1/2}
\end{aligned}
$$

Repeating the singular value decomposition for Γ_{i-1} is not necessary since it is related to Γ_i by removal of l rows. The state estimates may now be isolated using the right-inverse as before:

$$\hat{X}_i = \Gamma_i^{\textcircled{-1}} Y_f / Y_p, \quad \hat{X}_{i+1} = \Gamma_{i-1}^{\textcircled{-1}} Y_f^{-1} / Y_p^+$$

We now perform a least squares minimization to identify the plant matrices A and C according to the problem:

$$\begin{pmatrix} \hat{X}_{i+1} \\ Y_{i|i} \end{pmatrix} = \begin{pmatrix} A \\ C \end{pmatrix} \begin{pmatrix} \hat{X}_i \end{pmatrix} + \begin{pmatrix} \rho_w \\ \rho_v \end{pmatrix} \tag{5.6}$$

by omission of ρ_w and ρ_v which are the forward innovations and the remaining Kalman filter residuals [38]. They are also orthogonal to $\hat{X}_i$. We use the residuals next to identify the covariance and process noise:

$$\begin{pmatrix} Q & S \\ S^T & R \end{pmatrix} = \mathbf{E}_j [\begin{pmatrix} \rho_w \\ \rho_v \end{pmatrix} \begin{pmatrix} \rho_w & \rho_v \end{pmatrix}] \tag{5.7}$$

A Riccati equation is then solved which yields the Kalman filter gain (refer [38] for complete algorithm implementation); this leaves us with the forward innovation model:

$$\begin{aligned} x_{k+1} &= \hat{A} x_k + K e_k \\ y_k &= \hat{C} x_k + e_k \\ \mathbf{E}[e_k (e_k)^T] &= R \end{aligned} \tag{5.8}$$

Since we have modelled the system as a purely stochastic process for which $u_k = 0$, we do not have an B or a D as are typically found in state space models but are left with an analogous system wherein the noise signal e_k takes the job of exciting the system in place of u_k. We seek now to express (5.8) in a form more consistent with a state space system that is readily applicable for use as a weighting function in $\mathcal{H}_\infty$ control. We require the weighting function to be SISO which will be driven by a normalized excitation variable.

Let us define a noise variable:

$$e_b := \frac{e_k}{\sqrt{R}} \tag{5.9}$$

The covariance of our new noise signal is hence:

$$\begin{aligned} \mathbf{E}[e_b(e_b)^T] =& \mathbf{E}[\frac{e_k}{\sqrt{R}}(\frac{e_k}{\sqrt{R}})^T] \\ =& \frac{1}{R}\mathbf{E}[e_k(e_k)^T] \\ =& 1 \end{aligned} \tag{5.10}$$

Substituting e_b into (5.8) we have:

$$\begin{aligned} x_{k+1} =& Ax_k + K\sqrt{R}e_b \\ y_k =& Cx_k + \sqrt{R}e_b \\ \mathbf{E}[e_k(e_k)^T] =& 1 \end{aligned} \tag{5.11}$$

The I/O behaviour of (5.11) is identical to that of (5.8) subject to a modified excitation signal which has a unit covariance. We denote this system by $W_o(s)$ which serves as our model of the noise disturbance within the vehicular cabin. In performing our controller design, we can think of the noise signal e_b as an exogenous input signal which drives a standard state space model $W_o(s)$ for which we may readily incorporate in $\mathcal{H}_\infty$ synthesis to minimize the system norm and thereby minimize the impact that e_b has on the system error. For the purpose of simulation, it is necessary that we complete the analogy to think of the forward innovation model as a fixed state space system:

$$\begin{aligned} x_{k+1} =& \hat{A}x_k + \hat{B}u_k \\ y_k =& \hat{C}x_k + \hat{D}u_k \end{aligned} \tag{5.12}$$

where we define, $\hat{B} = K\sqrt{R}$, $\hat{D} = \sqrt{R}$ and $u_k = e_b$.

When this system is driven by a zero mean excitation signal u_k which has a unit covariance, it will produce an approximation of our noise disturbance which we have modelled. In the case of buffeting noise, for example, the low-frequency hammering sound which is characteristic of this noise type, is captured completely by the model in (5.12).

Implementation of the subspace identification algorithms was carried out using the N4SID algorithms published by Van Overschee and De Moor in the release of [38].

5.3 Decimation Factor Selection

In practice, using the fixed sampling frequency governed by the Freescale hardware platform of 44100 Hz, it was found that stochastic identification algorithms did not perform well. In analyzing the empirical buffeting data, the identification technique failed to capture the dynamics of the noise source to any degree. It was postulated that since most of the spectral energy contained in the noise models, such as buffeting, exists at low-frequencies with first harmonics at around 17 Hz; they fail to be detected by the identification algorithms which are operating at 44.1 kHz. Most of the dynamics of the system that we seek to capture are concentrated within a very low and narrow band of frequencies compared to the Nyquist ($\frac{F_s}{2}$) rate. The sampling frequency, fixed by a hardware configuration on the Freescale development board, is excessively high relative to the bands which we target for attenuation.

We opt to introduce a means to downsample the noise prior to introducing it to the stochastic identification block to ensure that the spectral energy is more evenly spread out among the sampling band. The effectiveness of downsampling in stochastic identification has been shown in [49].

We use a heuristic for selecting the optimal decimation factor that gives strongest weight to the peak energy in the frequency response. Our knowledge of the noise characteristics provides some insight into the expected shape of the of the frequency response which enables us to tailor our decimation factor selection. We begin by performing an FFT on the noise sample-set and selecting the frequency which contains the highest energy. If we are detecting buffeting, we know this fundamental tone will represent the first harmonic of the hammering sound:

$$\omega_c = \arg\max_{\omega} |\hat{N}(z)|_{z=e^{j\omega}} \tag{5.13}$$

Our objective is to find an optimal Nyquist frequency which is some multiple of w_c so as to ensure that most of the spectral contents of the noise are included. Once the new Nyquist frequency is found, we select the nearest decimation factor which divides evenly into F_s.

Figure 5.2 shows the effect of varying the decimation factor on the performance of the stochastic subspace identification algorithm. In performing the analysis, we begin with a demonstrative transfer function which is in the spectral range of the buffeting noise to serve as an example. We define a transfer function which is two cascaded second order systems with critical frequencies of 10 Hz and 100 Hz respectively in addition to several single order filters to balance the response. We use the same sampling rate as in the hardware platform, $F_s = 44.1$ kHz and iterate on the decimation factor subject to the criteria above.

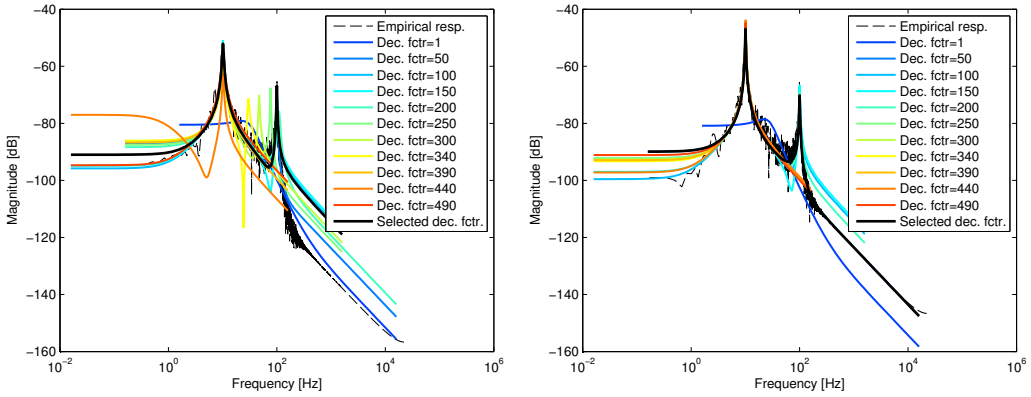

Fig. 5.2 Effect of decimation of on subspace identification performance in capturing sample plant model dynamics with varying decimation factor (a) No anti-aliasing filter used, (b) Approximation of ideal low-pass filter performing anti-aliasing before decimation.

Prior to performing the decimation, we pass an FIR low-pass filter over the data to remove the spectral components at frequencies greater than the decimation in a technique demonstrated by Boulet in [50]. An approximation of the sinc function is used here to pre-filter the data with a cut-off at $\frac{F_s}{2M}$, where M is the decimation factor.

As is evident in Figure 5.2, when the decimation factor is too small (e.g. Dec. fct=1), we see that the stochastic SSI totally fails to capture any significant characteristics of the system. The effectiveness of the anti-aliasing filter is also demonstrated in Figure 5.2; without the use of the pre-processing filter, aliasing occurs as the high frequency peaks are folded into the main spectra, as shown in (a). By introducing the anti-aliasing filter, as in (b), all aliasing artefacts are prevented. If the decimation factor is too large (e.g the Nyquist frequency shifted too low), the second peak at 100 Hz is lost completely as a result of anti-aliasing filter. The location of the Nyquist frequency which best captures

the system dynamics is found to occur, for this example, at x40 times the peak energy level. The corresponding decimation factor is chosen to be the next closest, even multiple of F_s subject to a downward search. We search downward, decreasing the decimation factor, to lessen the risk of losing information to anti-aliasing. For the purposes of this analysis, this heuristic makes sense from the perspective of buffeting since it will ensure that we downsample such that the Nyquist frequency is around twenty times greater than the fundamental tone which is typically around 17 Hz.

5.4 Effect of sampling window size

An additional parameter under analysis in the stochastic subspace identification algorithms is the window size used in collecting data. In the derivation of the stochastic SSI, one of the assumptions stated in [38] is that the number of sample points increase to infinity to ensure convergence of the model. Hence we ideally wish to perform our identification on a infinitely long sample-set. We are faced therefore, with a trade-off in which we wish to incorporate as many samples as possible to improve the model of the noise but are limited by the memory available within the DSP and additionally, the computation time associated with performing the identification for systems with increasing size. Figure 5.3 below shows the effect of the window size on the convergence of the stochastic model. To quantify the window size, we indicate the number of samples as a multiple of the sampling rate; for example, a window of size $4F_s$, where $F_s = 44100Hz$, contains 176,400 samples.

Here, we are performing the estimation on empirical test data of the buffeting at 100 km/h. The test is carried out by increasing the multiples of the sampling frequency F_s, which are used to set the sample window size, followed by the stochastic subspace identification operation. It should be noted that the units of this test are not in [SPL] as they were in Figure 5.1 but rather are the direct FFT of the samples. A sample size, N, that incorporates one sampling frequency F_s (or 44100 samples) yields a noise model which captures the dynamics of the frequency response loosely but it clearly too conservative given its magnitude exceeds that of all subsequent tests. We see that with increasing multiples of the sampling frequency, there is convergence such that $N = 5F_s$ is almost indiscernible from $N = 4F_s$. With the biggest change from $N = Fs$ to $N = 2Fs$, we select $N = 2Fs$ as a good compromise in window size against computational complexity. It should be noted that given the downsampling procedure outlined previously, a window size of $2F_s$ will ac-

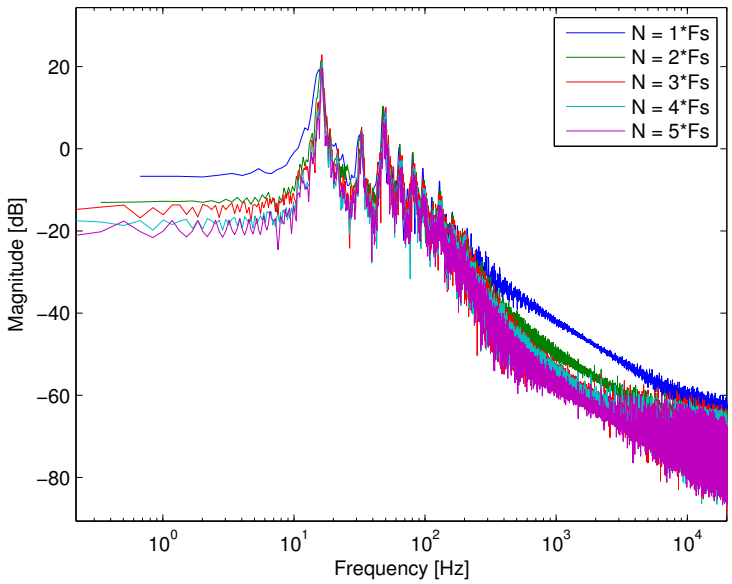

Fig. 5.3 Convergence of subspace identification model to true noise characteristics with increasing data windows by multiples of sampling rate, buffeting noise with increasing N sample points, Fs = 44100 Hz

tually contain substantially fewer than 88200 samples depending on the locale of the power density in the spectra. An in depth analysis of performing subspace identification on-board a DSP is detailed in [51].

5.5 Noise Estimator

In feedforward control, it was shown that measurements of the system's error, which represent noise which has not been attenuated, can be used to optimize the coefficients of a filter to improve the noise attenuation in the subsequent step. The error signal itself played no role in directly driving the actuator, instead, the noise signal itself was used filtered an served to drive the anti-noise actuator. In the method presented in this thesis, we perform the converse: the error signal is used to directly drive the actuator in a closed-loop feedback configuration, an estimation of the noise is used to improve the performance of the noise attenuation in the next step by *reducing uncertainty*. We therefore require a means to estimate the corrupting noise source. Let us consider the a model of the plant which includes the output disturbance:

The microphone is omitted from the model since we negate its presence on the DSP

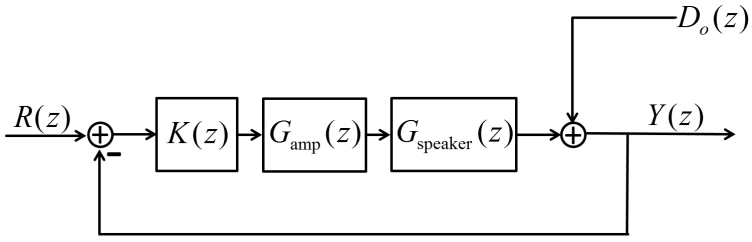

Fig. 5.4 Feedback control block diagram containing disturbance

by applying a virtual microphone inversion. This means that all units of the plant are in Pascals except for the voltage channels between the control, amplifier and speaker. Let us differentiate the true model of a plant from an internal estimate of the plant by invoking the tilde notation where, for example, $\widetilde{G}_{speaker}$ is our subspace identification model of the true plant, $G_{speaker}$. To isolate the noise, we begin with an internal model of the plant in Figure 5.4 which relies on our estimates of the plant parameters:

$$Y(z) = \frac{\widetilde{G}_{speaker}(z)\widetilde{G}_{amp}(z)K(z)}{1+\widetilde{G}_{speaker}(z)\widetilde{G}_{amp}(z)K(z)}R(z) + \frac{1}{1+\widetilde{G}_{speaker}(z)\widetilde{G}_{amp}(z)K(z)}D_o(z) \tag{5.14}$$

Our noise estimator is obtained by solving (5.14) for $D_o(z)$:

$$\hat{D}_o(z) = Y(z) - (R(z) - Y(z))\widetilde{G}_{speaker}(z)\widetilde{G}_{amp}(z)K(z) \tag{5.15}$$

We may equivalently give (5.15) in the time domain. A particular noise sample is computed by:

$$\begin{aligned} \hat{d}_{ok} &= y_k - (r_k - y_k) * b \\ \text{where } b &= \mathcal{Z}^{-1}\{\widetilde{G}_{speaker}(z)\widetilde{G}_{amp}(z)K(z)\} \end{aligned} \tag{5.16}$$

Our noise estimator, creates a stream of samples derived from the difference between the system output, measured by the microphone, and the error signal weighted by convolution with the plant and controller dynamics. This estimation of the noise is useful because it removes the effect of any noise cancellation which may have made other noise measurement techniques difficult. It should be noted however, that it is crucial that the open-loop plant and controller model be stable hence by extension, it is only applicable to systems in which the poles of $\widetilde{G}_{speaker}(z)$, $\widetilde{G}_{amp}(z)$ and $\widetilde{K}(z)$ are contained within the unit circle. For most

open-loop acoustic systems, this requirement is satisfied. Another point worth mentioning is our reliance on the accuracy of the plant estimates.

The interconnection of $\widetilde{G}_{speaker}(z)\widetilde{G}_{amp}(z)K(z)$ is referred to in literature as the extended plant model. It is used extensively in internal model control (IMC) [52] which may theoretically achieve perfect attenuation barring omission of physical limitations [53]. In fact, the use of the IM has been used for disturbance rejection which was first demonstrated rigourously in [54] for cancellation of a deterministic noise source.

Implementation of our noise estimator is carried out in Simulink$^{\text{TM}}$as shown in Figure 5.5 which also approximates how such a process is executed onboard a DSP. The signal from the microphone, which measures the audio levels in the cabin, is sampled onto the DSP where it is converted into a quantized digital signal. We invert the gain of the sensor by applying a virtual microphone inversion so that our units are consistent in Pascals. Similarly, the reference signal containing either a musical sample or pure silence are also fed into the estimation block and subject to virtual microphone inversion.

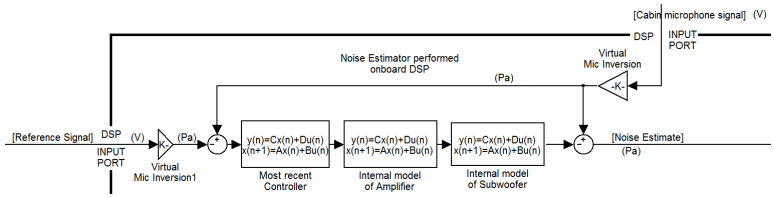

Fig. 5.5 Block diagram of noise estimator internal to DSP for extracting noise characteristics from output measurements.

Our internal model then processes the error signal to advance forward by one time-step; its output is subtracted from the sound measured in the cabin and the result is an approximation of the noise. The stream of noise samples constitute the input to the stochastic subspace identification block which, as explained, creates a model of the plant disturbance.

It will be demonstrated in Section 6.1.1 how the noise model is incorporated into the control design as a weighting function, however, let us state now that the phase of such functions can be ignored [53]. But we do require however, that the weighting functions be stable and some biproper. The phase invariance is beneficial since it allows for simple post-processing of the model to quickly reflect all non-minimum phase zeros and unstable poles into the OLHP which does not impact magnitude characteristics.

5.6 Noise Simulation

To verify the performance of the controller which is computed in the next section, we require a means to subject the feedback control system to varying disturbance conditions. In the real-world, these simulations represent changes in the environment such as opening or closing a window, increasing speed, decreasing speed or changes to the RPM of the engine. It is our objective to confirm that the controller behaves expectedly in these scenarios by adapting as required.

For reasons that could not be determined throughout the course of this investigation, a unit discrepancy was introduced by the stochastic noise models which caused the amplitudes of their respective outputs (when excited by a zero-mean, unit covariance input) to be less than the noise measured in the vehicle. While the shape of the frequency response was indeed very accurate indicating the harmonics were present in the right proportion, the magnitude was significantly smaller. While the decimation may be partially attributed to gain offset, the source of the energy loss could not be accounted for entirely. Through trial and error, a correction factor of 874 was deemed ideal to adjust the units to match those which were recorded in the tests. With this constant factor, all models produced through the stochastic SSI algorithms yielded simulation outputs which matched the empirical data very well. Figure 5.6 shows the simulation block which is used for synthesizing vehicular cabin noise representative of ambient highway driving at 100 km/h and the buffeting phenomenon at 100 km/h when the front passenger window was opened. The noise models were excited by a zero mean Gaussian noise with covariance equal to 1, consistent with (5.12). For completeness, the system is also simulated direct noise samples collected from empirical tests.

Programmable noise source selection is performed by the multiport switch shown in Figure 5.7. Simulations using varying sequences of noise transitions are used to demonstrate the effectiveness of the feedback control loop in adapting to changes in output disturbance.

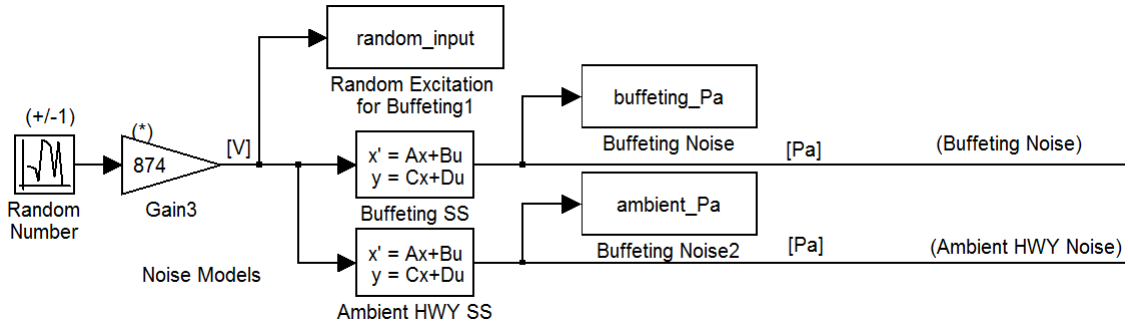

Fig. 5.6 Simulation setup for noise creation; white noise is generated and its variance adjusted to adjust the output units. Passing through the transfer function models of the empirical noise, the specific characteristics for highway driving window and buffeting noise respectively are added.

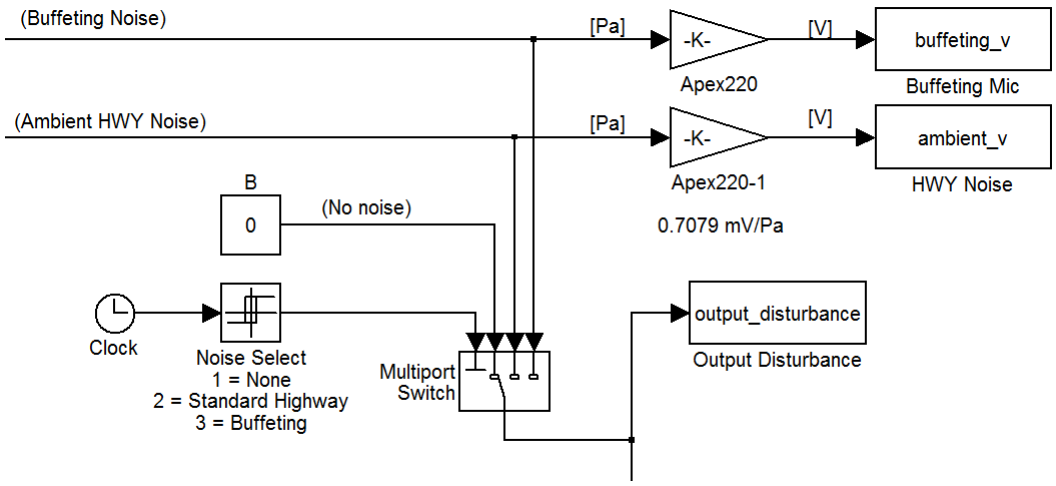

Fig. 5.7 Noise selection block for simulating transitions between buffeting, highway ambient and zero-noise output disturbance.

Chapter 6

Controller Design & Simulation

We now proceed to perform the control design to perform the task of active noise control which we have been building towards. Once the controller has been created, we will design a state machine to update the controller with up-to-date models of the disturbance. Finally, we simulate the system and discuss the results

6.1 $\mathcal{H}_\infty$ synthesis

6.1.1 Principle of $\mathcal{H}_\infty$ Control

$\mathcal{H}_\infty$ synthesis is a control strategy which minimizes the maximum gain of a closed-loop system with a stabilizing LTI controller. Prior to stating the theorems of the theory, we briefly review the concept of a norm. A norm an operation performed on bounded functions which assigns a non-negative number to the manner in which the function transforms input to output. The most familiar norm is the Euclidian, or L^2 which represents the length of a vector in a given space. We may produce a norm using an exponent other than 2, however, in fact the general norm is referred to as the p-norm and is given by:

$$\left\| f \right\|_p := (\int_D |f|^p \, \mathrm{d}\mu)^{1/p} \tag{6.1}$$

or equivalently in the discrete domain by:

$$\left\| X \right\|_p := (\sum_{i=0}^{n} |x_i|^p)^{1/p} \tag{6.2}$$

The most oft used norms consist of $p = 1$ which is the sum of the element magnitudes, $p = 2$ which is the Euclidian norm, and $p = \infty$ which is equivalent to:

$$\left\| X \right\|_{\infty} := \max \{|x_1|, |x_2|, \ldots, |x_n|\} \tag{6.3}$$

In the context of LTI systems, norms provide us with a measure of the system's gain. The $\mathcal{H}_2$-norm can be interpreted as quantitative metric of the energy in the impulse response and analogous to the RMS; this norm can be defined by:

$$\left\| H \right\|_2 := (\frac{1}{2\pi} \int_{-\infty}^{\infty} trace\{H(j\omega)^* H(j\omega)\} \, \mathrm{d}\omega)^{1/2} \tag{6.4}$$

Our interest, however, is on the $\mathcal{H}_\infty$-norm which is interpreted as the *maximum gain* of the system. To properly understand the infinity norm of a linear system, let us first introduce the spectral norm which is defined as the maximum singular value $\bar{\sigma}$:

$$\left\| H \right\| = \bar{\sigma}(H) = [\lambda_{max}(H^* H)]^{\frac{1}{2}} \tag{6.5}$$

where $(^*)$ denotes the complex conjugate and λ_{max} is the largest eigenvalue. Here, the spectral norm represents the maximum input-output gain of the 2-norms of the respective input and output vectors [53]. The $\mathcal{H}_\infty$-norm is then given by:

$$\begin{aligned} \left\| H \right\|_{\infty} &= \sup_{\omega \in \mathbb{R}} \{\bar{\sigma}(H(j\omega))\} \\ &= \sup_{\omega \in \mathbb{R}} \left\| H(j\omega) \right\| \end{aligned} \tag{6.6}$$

Hence the $\mathcal{H}_\infty$-norm of a system H, is the maximum gain between an input-output pair of $\mathcal{L}_2$ bounded signals across *all* frequencies; it can be found by identifying the peak amplitude of the system's Bode plot. This norm is especially useful for noise attenuation because it allows us to control the limit by which a signal is amplified from an input to the output. If we recast our system to consider the noise disturbance as an input, we can utilize the tools of $\mathcal{H}_\infty$ synthesis to limit the impact of the noise on the system output.

Let us formulate our system as linear fractional transformation (LFT) where all known systems are included into an augmented plant P and our controller is removed and isolated outside of the plant as in Figure 6.1(a). We introduce now a new notation for vectors

using the horizontal arrow; this notation represents a vector of input/output signals which, themselves, contain vectors indexed in time. In addition to the I/O connections from the external controller, our augmented plant has an input vector $\vec{w}$ and output vector $\vec{z}$. The infinity norm which we shall control is that of the transfer function $T_{w \mapsto z}$ and hence we create interconnections between $\vec{w}$ and $\vec{z}$ according to norms that we set out to minimize. For our purposes, we achieve our objective by including in the input vector $\vec{w}$ the signals $d_o(s)$, $d_i(s)$, and $y_r(s)$ to represent output disturbance, input disturbance and reference signal respectively. Included in the output vector $\vec{z}$ are signals $\widetilde{u}(s)$ and $\widetilde{e}(s)$ to represent weighted control and error signals respectively. A description of the weighting functions $W_o(s)$, $W_i(s)$, $W_u(s)$ and $W_e(s)$ is postponed until after the general $\mathcal{H}_\infty$ problem has been formulated.

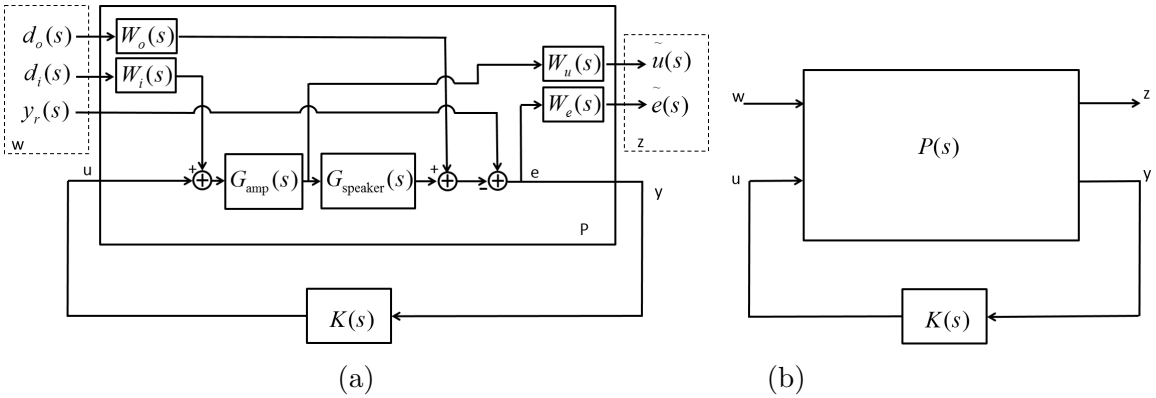

Fig. 6.1 (a) Piezoelectric speaker system recast into linear fractional transformation, (b) Standard LFT form for $\mathcal{H}_\infty$ problem.

The system is now in LFT form as in Figure 6.1(b), where $P(s)$ is referred to as the generalized plant which contains the transfer matrix entries:

$$P(s) = \begin{bmatrix} P_{11}(s) & P_{12}(s) \\ P_{21}(s) & P_{22}(s) \end{bmatrix} \tag{6.7}$$

This relates to the following sets of equations:

$$\begin{aligned} z(s) &= P_{11}(s)\vec{w}(s) + P_{12}(s)\vec{u}(s) \\ y(s) &= P_{21}(s)\vec{w}(s) + P_{22}(s)\vec{u}(s) \end{aligned} \tag{6.8}$$

where the transfer matrices are given by:

$$\begin{aligned}
P_{11}(s) &= \begin{bmatrix} 0 & W_i(s)G_{amp}(s)W_u(s) & 0 \\ -W_o(s)W_e(s) & -W_i(s)G_{amp}(s)G_{spkr}(s)W_e(s) & W_e(s) \end{bmatrix} \\
P_{12}(s) &= \begin{bmatrix} G_{amp}(s)W_u(s) \\ -G_{amp}(s)G_{spkr}(s)W_e s \end{bmatrix} \\
P_{21}(s) &= \begin{bmatrix} -W_u(s) & -W_i(s)G_{amp}(s)G_{spkr}(s) & 1 \end{bmatrix} \\
P_{22}(s) &= \begin{bmatrix} -G_{amp}(s)G_{spkr}(s) \end{bmatrix}
\end{aligned} \tag{6.9}$$

Given $P(s)$, we seek to synthesize a controller $K(s)$ which minimizes the $\mathcal{H}_\infty$-norm of the closed loop transfer function from the exogenous input vector $\vec{w}(s)$ to output vector $\vec{z}(s)$. The closed loop transfer function is given by the lower LFT. The objective can be summarized as follows:

$$\min_K \left\| T_{zw} \right\|_\infty \tag{6.10}$$

where:

$$\begin{aligned}
T_{zw} =& \mathcal{F}_L[P(s), K(s)] \\
=& P_{11}(s) + P_{12}(s)K(s)[I - P_{22}(s)K(s)]^{-1}P_{21}(s)
\end{aligned} \tag{6.11}$$

$\mathcal{H}_\infty$ synthesis finds a suboptimal solution to this problem since optimizing (6.10) is not typically feasible given computational limitations. The solution takes the form of selecting a $\gamma > 0$ and attempting to find an admissible controller such that $\left\| T_{zw} \right\|_\infty < \gamma$. This inequality can be solved closed-form and requires only the solution to two algebraic Riccati equations [55]. If a suitable controller is found, we identify the smallest permissible γ using the bisect method until the suboptimal controller is found. The conditions and assumptions required to find an admissible controller can be found in [53, 55].

Incorporation of the weighting functions $W_o(s)$, $W_i(s)$, $W_u(s)$ and $W_e(s)$, which were introduced into our FLT plant, is crucial in exploiting the power of $\mathcal{H}_\infty$ synthesis as it enables direct loop-shape control of the infinity norm. Suppose that we have identified a $\gamma > 0$ for which an admissible controller $K(s)$ has been produced, this results in stable

closed-loop transfer function with $\left\|T_{zw}\right\|_\infty < \gamma$. This result can also be expressed as:

$$\left\| \begin{bmatrix} d_o \\ d_i \\ y_r \end{bmatrix} \mapsto \begin{bmatrix} \widetilde{u} \\ \widetilde{e} \end{bmatrix} \right\|_\infty < \gamma \quad \Rightarrow \quad \left\| d_o \mapsto \widetilde{e} \right\|_\infty < \gamma \tag{6.12}$$

$$\therefore \quad |T_{d_o \mapsto \widetilde{e}}(j\omega)| < \gamma, \quad \forall \omega \tag{6.13}$$

From our block diagram in Figure 6.1(a), we compute $T_{d_o \mapsto \widetilde{e}}(j\omega)$ as:

$$T_{d_o \mapsto \widetilde{e}}(j\omega) = \frac{1}{1 + G_{spkr}(j\omega)G_{amp}(j\omega)K(j\omega)} W_e(j\omega)W_o(j\omega) \tag{6.14}$$

So given the result in (6.13) we have:

$$\left| \tfrac{1}{1+G_{spkr}(j\omega)G_{amp}(j\omega)K(j\omega)} W_e(j\omega)W_o(j\omega) \right| < \gamma \tag{6.15}$$

$$\left| \tfrac{1}{1+G_{spkr}(j\omega)G_{amp}(j\omega)K(j\omega)} \right| < \left| \gamma W_e^{-1}(j\omega)W_o^{-1}(j\omega) \right| \tag{6.16}$$

The presence of γ in (6.16), provides insight into whether or not we have achieved our objective. A $\gamma > 1$ indicates that the closed-loop infinity norm has exceeded that which we intended; or in other words, our sensitivity has violated a constraint at some point its Bode plot. Ideally, we seek to find an admissible controller $K(s)$ which yields a $\gamma < 1$. To demonstrate this, suppose that we let $\gamma = 1$ in (6.16), we then have:

$$\left| \tfrac{1}{1+G_{spkr}(j\omega)G_{amp}(j\omega)K(j\omega)} \right| < \left| W_e^{-1}(j\omega)W_o^{-1}(j\omega) \right| \tag{6.17}$$

which implies that the system sensitivity is less than $W_e^{-1}(j\omega)W_o^{-1}(j\omega)$ at all frequencies. In contrast, if $\gamma > 1$ then we must scale the sensitivity by a factor γ to ensure that it remain less than $W_e^{-1}(j\omega)W_o^{-1}(j\omega)$.

By selecting an appropriate frequency response for the weighting functions, we can limit the maximum closed-loop gain of the sensitivity (and related constraints) on a frequency by frequency basis. Without the use of weighting functions, a minimum $\mathcal{H}_\infty$-norm is still achieved, however the norm is the same for all frequencies and does not afford us any control in tailoring the specific $\mathcal{H}_\infty$-norm at a specific frequency.

The result in (6.16) shows that we can directly control the impact that the output disturbance d_o will have on the interior of the vehicular cabin. The noise disturbance, whose dynamics are captured by $W_o(s)$, is computed directly from the stochastic subspace identification algorithm which derives its excitation signal from our noise estimator. The result is that we have a decreased uncertainty in the disturbance that our system faces which allows to more precisely optimize our controller and achieve improved performance. By selecting an appropriate $W_e^{-1}(s)$ and given that $W_o^{-1}(s)$ is stable and minimum phase (through the reflection of any ORHP poles and zeros to the OLHP to preserve magnitude-only), we may theoretically achieve perfect noise attenuation. In reality, we are limited by many factors including saturation limits of the control hardware and the piezoelectric subwoofer actuator; further, the model approximations that were made by removing the NMP zeros in section 4.1, effectively negated the propagation delay of sound. While we attempted to improve this approximation with lead-lag compensation, it is acknowledged that the true system would contain such NMP components. We shall now proceed to discuss the process of selecting appropriate weighting functions.

6.1.2 Weighting function: output disturbance

The output disturbance weighting function $W_o(s)$ describes the spectral contents of the output disturbance [53]. We derive its transfer function directly from the stochastic subspace identification algorithm after the noise estimator processes the measurements of the microphone. Unstable modes and non-minimum phase zeros are reflected into the ORHP without consequence since it is only the magnitude of the weighting functions which affect the $\mathcal{H}_\infty$ synthesis and the feasibility of identifying an admissible controller.

6.1.3 Weighting function: error

As stated, we are provided with direct control over the impact of the disturbance output has on our system through the product of $W_e^{-1}(s)W_o^{-1}(s)$. The weighting function $W_o(s)$ is beyond our control since it represents a real disturbance bombards the cabin of the vehicle. The error weighting function $W_e(s)$ however, is completely user-defined and must be selected carefully to achieve the desired closed-loop behaviour. An admissible controller may not be achievable, for example, without some scaling of $W_o(s)$ to limit its impact on the sensitivity that $\mathcal{H}_\infty$ synthesis attempts to achieve. We now describe the technique for

selecting $W_e(s)$ adaptively, depending on the disturbance which the system faces.

First let us consider which $\mathcal{H}_\infty$-norms are affected by the selection of $W_e(s)$:

$$T_{d_o \mapsto e} = \frac{1}{1 + G_{spkr}(s)G_{amp}(s)K(s)} W_e(s)W_o(s) \tag{6.18}$$

$$T_{y_r \mapsto e} = \frac{-1}{1 + G_{spkr}(s)G_{amp}(s)K(s)} W_e(s) \tag{6.19}$$

$$T_{d_i \mapsto e} = \frac{G_{spkr}(s)G_{amp}}{1 + G_{spkr}(s)G_{amp}(s)K(s)} W_e(s)W_i(s) \tag{6.20}$$

We may omit (6.20) since $W_i(s)$ serves primarily to aide in numerical stability when solving for $K(s)$ and so the influence of $d_i(s)$ can be safely ignored. Hence $W_e(s)$ impacts both our disturbance rejection and our referencing tracking. Conveniently, the transfer functions for both of these objectives are represented by the closed-loop sensitivity so our objective to attenuate disturbance can be carried out with our objective in flattening the acoustic response of the subwoofer simultaneously.

However, to consider a single sensitivity function objective for *all* environmental conditions requires that we minimize the $\mathcal{H}_\infty$-norm of our system when the ambient noise is small and when it faces aggressive noise disturbance from window buffeting simultaneously in the same way. This objective implies that we seek to obtain the same high-fidelity musical reproduction both when the windows are closed, at which time the passengers' can pay close attention to the acoustic response, and when the window is open at which time the buffeting phenomenon severely detracts from the passengers' ability to hear the music at all. Further, it implies that there is wide uncertainty contained in the model for $W_o(s)$ since it must cover the worst case of all possible noise disturbances.

When the window buffeting is engaged, the average noise level within the vehicular cabin increases drastically such that our interest in high-fidelity audio becomes less important compared to the more pertinent noise disturbance which fills the cabin. In some instances, it was found that performance could be improved by identifying the harmonics alone within the noise and tailoring a notch filter directly into $W_e(s)$, however, for the purpose of this investigation we will not discuss those results further.

When there is only ambient highway noise, broadband noise attenuation and high-fidelity music reproduction can be achieved simultaneously. But in the presence of buffeting, we opt to shift the control objective to more aggressively target the buffeting phenomenon.

While applying broadband noise attenuation to target buffeting will effectively reduce its volume, the controller's ability to have a significant impact on the cancellation of the harmonics is limited due to the so-called waterbed effect imposed by Bode's sensitivity integral [56] which states that:

$$\int_0^\infty \ln|S(j\omega)|d\omega = 0 \tag{6.21}$$

Given that the sensitivity integral must be equivalent to unity, broadband attenuation reduces our ability to apply more aggressive attenuation to a single frequency. A decreased sensitivity at one frequency results in increased sensitivity at another. With a finite *quantity* of attenuation possible, subject to the constraint's of Bode's sensitivity integral, it can be interpreted as *wasteful* for us to attenuate frequencies which are not as detrimentally impacting our system while critical harmonics in buffeting are more directly causing passenger discomfort. Through simulation, it is found that the harm done by trying to severely attenuate buffeting harmonics whilst simultaneously providing broadband disturbance rejection results in increased sensitivity at (typically) higher frequencies. This is perceived by the passenger as high frequency static noise. Hence in the presence of buffeting, our approach is to reduce broadband noise cancellation and increase the notch attenuation whereby independent frequencies are attenuated more drastically.

Conversely, to incorporate good frequency notching into the sensitivity function that we use for the high-fidelity musical playback results in undesirable auditory effects since the acoustic response is no longer flat.

Our periodic re-modelling of the noise disturbance through implementation of the stochastic subspace identification algorithm provides us with insight into how and when this trade-off needs to be re-optimized.

We control the disturbance's maximum impact on our error by using W_e^{-1} to control our broadband attenuation and W_o^{-1} to directly incorporate the stochastic model of our noise into the optimization. When buffeting noise is detected, we proceed to increase W_e^{-1} (lessen the system's requirement to achieve broadband attenuation) and W_o^{-1} is scaled to achieve as much buffeting rejection as possible. Direct use of $W_o(s)$ was found to yield some success.

In times of ambient highway disturbance, $W_o(s)$ becomes so small that we may effectively omit and instead, use $W_e(s)$ alone to implement ANC. We flatten the acoustic

response of the piezoelectric subwoofer by controlling its transmission function, which is given by the complementary sensitivity:

$$T(s) = \frac{G_{spkr}(s)G_{amp}K(s)}{1 + G_{spkr}(s)G_{amp}(s)K(s)} \tag{6.22}$$

The complementary sensitivity describes transfer function of the input reference music signal to the output, as in $T_{y_r \mapsto y_o}$. Transmission is the specification most often cited for the auditory characteristics of a speaker since it describes how frequencies are amplified in the bandwidth of operation. Competing subwoofer installations were researched and their transmission functions used to establish a reasonable transmission function. The specific competitors are not indicated here, but the nature of this control design process is that the transmission characteristics may be modified or tuned to the taste of the end-user. With the transmission function described, we may deduce the desired sensitivity through the use of the identity:

$$T(s) = I - S(s) \tag{6.23}$$

where $S(s)$ is the sensitivity. Hence from the transmission, we may directly deduce the targeted sensitivity. We formulate the transmission specification in the context of $\mathcal{H}_\infty$ design as:

$$\begin{aligned} \left\| T_{y_r \mapsto e} \right\|_\infty &< \gamma \\ \left\| \tfrac{-1}{1+G_{spkr}(s)G_{amp}(s)K(s)} W_e(s) \right\|_\infty &< \gamma \\ \left\| S(s) \right\|_\infty &< \gamma \left\| W_e^{-1}(s) \right\|_\infty \\ |S(j\omega)| &< \gamma |W_e^{-1}(j\omega)|, \quad \forall\omega \end{aligned} \tag{6.24}$$

Therefore by setting:

$$W_e^{-1}(s) = I - T(s) \tag{6.25}$$

we achieve the desired result. Some additional modifications to $W_e(s)$ is required to ensuring that the $\mathcal{H}_\infty$ problem is well posed.

6.1.4 Weighting function: actuator constraint

One of the limitations mentioned in section 6.1.1 is the physical realization of the control system hardware which contains amplifiers and speakers that experience saturation if they are overdriven. We can account for the saturation limit of the amplifier using the $W_u(s)$ weighting function. The closed-loop path which represents the transfer function from the input reference signal y_r and output disturbance d_o to the amplifier output are denoted by $T_{d_o \mapsto u}$ and $T_{y_r \mapsto u}$ respectively are given by:

$$T_{d_o \mapsto u} = \frac{G_{amp}(s)K(s)}{1 + G_{spkr}(s)G_{amp}(s)K(s)} W_o(s)W_u(s) \tag{6.26}$$

$$T_{y_r \mapsto u} = \frac{G_{amp}(s)K(s)}{1 + G_{spkr}(s)G_{amp}(s)K(s)} W_u(s) \tag{6.27}$$

We can therefore utilize $W_u^{-1}(s)$ to place a limit on the actuator constraint. The amplifier in the laboratory setup has a DC bias of approximately +90 V and allows for the peak-to-peak output of around +180 V, hence we set $W_u(s) = 1/90$ to impose a reasonable constraint on the amplifier output.

6.1.5 Synthesis

Synthesis of the $\mathcal{H}_\infty$ controller is performed in MATLAB$^{\text{TM}}$using the algorithms associated with the Robust Control Toolbox$^{\text{TM}}$. It is expected that γ values would not approach the desirable value of 1 however, initially tests showed failure in the identification of an admissible controller. Transfer function selection is non-trivial for a good controller design and hence the system's ability to converge immediately is not expected. Once admissible controllers are identified, values of γ larger than 1 indicate that violations in the $\mathcal{H}_\infty$-norm subject to the constrains of the weighting functions are present. To visually comprehend the nature of the violation, it is useful to create Bode plots to identify the precise location of the norm violation since the infinity norm is given by the peak magnitude of the plot. Consider for example, the result in (6.16) restated below, and suppose that the violation has occurred in this constraint:

$$\left| \frac{1}{1+G_{spkr}(j\omega)G_{amp}(j\omega)K(j\omega)} \right| < \left| \gamma W_e^{-1}(j\omega)W_o^{-1}(j\omega) \right|$$

When the bisection method converges, the magnitude of the sensitivity on the left of (6.16) touches that of the constraint on the right at the point which prevents a further decrease in γ. By setting $\gamma = 1$ and plotting (6.16), the full extent of the limiting constraint is shown by any section in the Bode plot where the magnitude of the sensitivity exceeds that of the constraint.

Through this method, the limiting components are identified by amplifier saturation and speaker gain. Given that the laboratory apparatus contains only a single piezoelectric mechanism while vehicular installations have on order of 2 or 4 actuators, the constraint was relaxed by allowing the speaker to operate louder than it was found possible in the lab. The assumption is made that with the addition of the multiple actuators and improvements in the amplifier driver, we can obtain a speaker which is capable of producing a 20 dB of sound. The second limiting constraint is that of the amplifier saturation. Amplifiers used in the modern implementations of the piezoelectric speaker have significantly higher voltage gain than that which was used in the lab, with the limiting factor being the dielectric properties of piezoelectric actuator and stroke length permissible by sealants. Our assumption then is to allow for a 400 V peak-to-peak signal. We believe this assumption is reasonable, however, we also acknowledge that these assumptions impact the feasibility for direct physical implementation.

The results of the modified tests are shown in the subsequent figures. Two optimizations are performed to present results indicative of the expected behaviour of the controller under buffeting conditions where notched disturbance rejection of the buffeting tones is the control objective, and under ambient highway noise conditions where high-fidelity acoustic linearity is the control objective.

Figures 6.2, 6.3, and 6.4 show optimization constraints plotted against the closed-loop infinity norm attained by the controller for the indicated transfer function. The constraint for broadband noise attenuation and associated reference tracking is relaxed to achieve better filtering of the noise harmonics without too significantly deteriorating the sensitivity at higher frequencies. Still, the waterbed effect is present as demonstrated by Figures 6.3(b) and 6.3(a) where the sensitivity exceeds 1 for some frequencies over 200 Hz. The γ value was greater than zero which is made obvious by the violations in Figure 6.3(b) which represents the transfer function from the output disturbance to the error. Here, we see that the first harmonic of the buffeting peak violated the capacity of the system. Despite the violation, all eigenvalues of the closed-loop system exist in the OLHP hence the system is

stable.

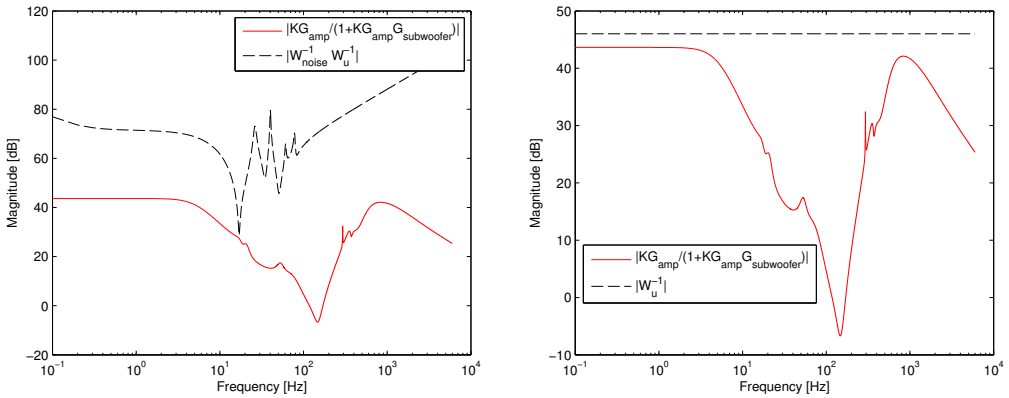

(a) $d_o \mapsto u \Rightarrow$ $|\frac{KG_{amp}}{1+KG_{amp}G_{subwoofer}}|_\infty < |W_{noise}^{-1}W_u^{-1}|$

(b) $y_d \mapsto u \Rightarrow$ $|\frac{KG_{amp}}{1+KG_{amp}G_{subwoofer}}|_\infty < |W_u^{-1}|$

Fig. 6.2 $\mathcal{H}_\infty$ optimization for buffeting disturbance, constraints for $d_o \mapsto u$ and $y_d \mapsto u$

Figures 6.5, 6.6, and 6.7 show the same constraint-sensitivity plots for the second synthesis which demonstrates the system's behaviour when the windows are closed. Experiencing only ambient highway noise, the control objective is switched to improve the acoustic linearity of the piezoelectric speaker and simultaneously perform broadband noise attenuation. We see again that a γ value less than one could not be achieved with reference to the controller saturation in Figure 6.5(b) at frequencies below 10 Hz. Since this plot represents the closed-loop transfer function of the reference signal to the controller output, we do not expect to excite the system in this band hence this violation is reasonable. We also see a violation in Figure 6.7(a) suggesting that the controller cannot fully achieve the closed-loop transmission that we sought, however, the desirable flat acoustic response is achieved. Evidence of the waterbed effect is also present here as the sensitivity exceeded 0 dB at frequencies outside of the bandwidth under study. Increasing the magnitude of $W_e^{-1}(s)$ to level of the sensitivity shown in Figure 6.7(a) resulted in an unexpected increase in the closed-loop sensitivity: it seems to obtain the flat acoustic response, we require the constraining $W_e(s)$ to exceed the capacity of the system. This behaviour is not well understood. All eigenvalues of the closed-loop polls are OLHP stable as was the case with for the buffeting disturbance.

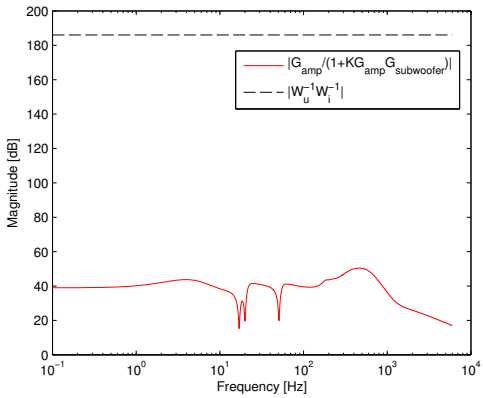

(a) $d_i \mapsto u \Rightarrow$
$|\frac{G_{amp}}{1+KG_{amp}G_{subwoofer}}|_\infty < |W_u^{-1}W_i^{-1}|$

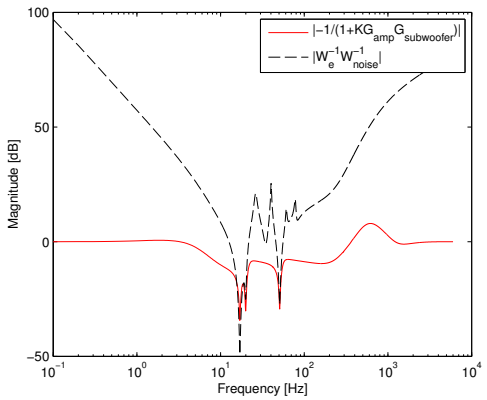

(b) $d_o \mapsto e \Rightarrow$
$|\frac{-1}{1+KG_{amp}G_{subwoofer}}|_\infty < |W_e^{-1}W_{noise}^{-1}|$

Fig. 6.3 $\mathcal{H}_\infty$ optimization for buffeting disturbance, constraints for $d_i \mapsto u$ and $d_o \mapsto e$

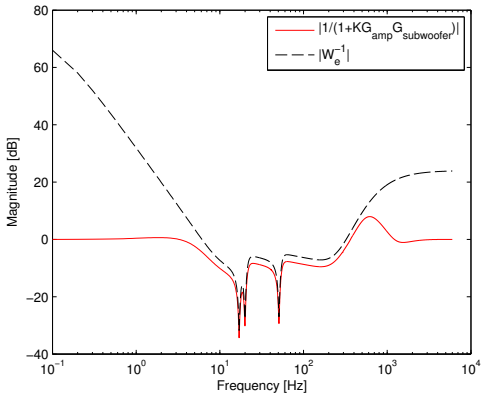

(a) $y_d \mapsto e \Rightarrow$
$|\frac{1}{1+KG_{amp}G_{subwoofer}}|_\infty < |W_e^{-1}|$

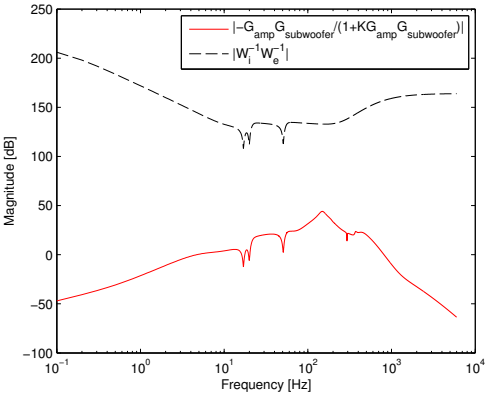

(b) $d_i \mapsto e \Rightarrow$
$|\frac{-G_{amp}G_{subwoofer}}{1+KG_{amp}G_{subwoofer}}|_\infty < |W_i^{-1}W_e^{-1}|$

Fig. 6.4 $\mathcal{H}_\infty$ optimization for buffeting disturbance, constraints for $y_d \mapsto e$ and $d_i \mapsto e$

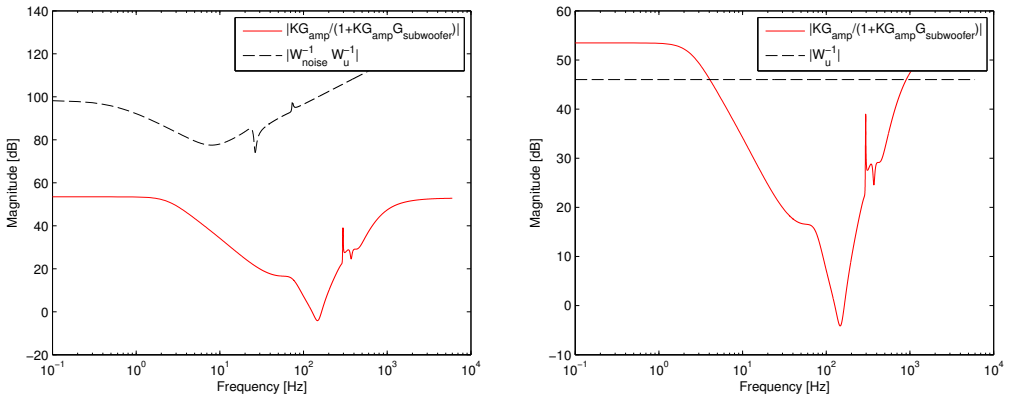

(a) $d_o \mapsto u \Rightarrow$ $|\frac{KG_{amp}}{1+KG_{amp}G_{subwoofer}}|_\infty < |W_{noise}^{-1}W_u^{-1}|$

(b) $y_d \mapsto u \Rightarrow$ $|\frac{KG_{amp}}{1+KG_{amp}G_{subwoofer}}|_\infty < |W_u^{-1}|$

Fig. 6.5 $\mathcal{H}_\infty$ optimization for ambient highway disturbance, constraints for $d_o \mapsto u$ and $y_d \mapsto u$

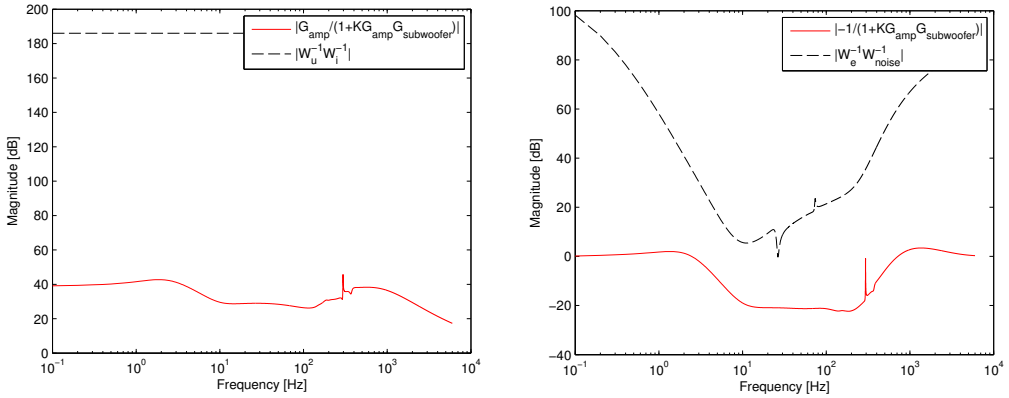

(a) $d_i \mapsto u \Rightarrow$ $|\frac{G_{amp}}{1+KG_{amp}G_{subwoofer}}|_\infty < |W_u^{-1}W_i^{-1}|$

(b) $d_o \mapsto e \Rightarrow$ $|\frac{-1}{1+KG_{amp}G_{subwoofer}}|_\infty < |W_e^{-1}W_{noise}^{-1}|$

Fig. 6.6 $\mathcal{H}_\infty$ optimization for ambient highway disturbance, constraints for $d_i \mapsto u$ and $d_o \mapsto e$

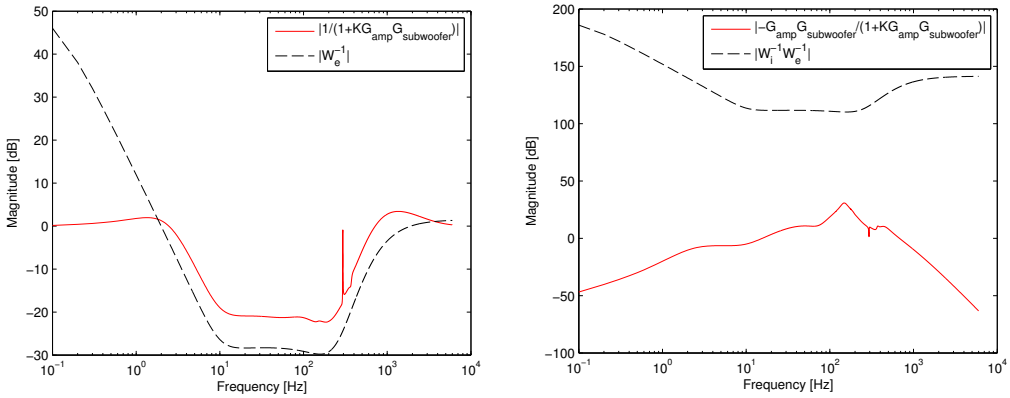

(a) $y_d \mapsto e \Rightarrow |\frac{1}{1+KG_{amp}G_{subwoofer}}|_\infty < |W_e^{-1}|$

(b) $d_i \mapsto e \Rightarrow |\frac{-G_{amp}G_{subwoofer}}{1+KG_{amp}G_{subwoofer}}|_\infty < |W_i^{-1}W_e^{-1}|$

Fig. 6.7 $\mathcal{H}_\infty$ optimization for ambient highway disturbance, constraints for $y_d \mapsto e$ and $d_i \mapsto e$

6.2 State machine

We utilize a state machine to implement our control strategy since it enables the deterministic operation that can be easier to debug. Figure 6.8 below shows the state machine used to determine when to appropriately perform stochastic SSI and to update the controller. The states may be summarized as follows:

State 0

Initialize the system and set the controller $K(s)$ to utilize the results from the optimization which yielded the high-fidelity acoustic response and broadband noise attenuation. Transition to state 1.

State 1

Once the system is activated, we begin our noise estimator functional block which uses the internal model of the plant to generate an estimate of the noise in the system $\hat{n}(k)$. The noise level in the vehicular cabin is monitored with an approximation of a windowed moving average $\hat{N}_{avg}$ of length L. At each noise sample, we perform the following update

to our estimate of the average noise:

$$\hat{N}_{avg}(k+1) = \hat{N}_{avg}(k) - \frac{\hat{N}_{avg}(k)}{L} + \frac{|\hat{n}(k)|}{L} \tag{6.28}$$

When the noise accumulates a $\hat{N}_{avg}(k)$ which exceeds some threshold (in simulations, this threshold is 10), we proceed to state 2.

State 2

Without changing the controller, we now begin buffering the noise samples. When we have collected a sufficient number of noise samples subject to the results in section 5.4, we perform stochastic subspace identification. During the computation of the SSI identification, we may continue to collect samples in case our controller does not successfully update. Once we have obtained our new noise model $W_o(s)$ we perform $\mathcal{H}_\infty$ synthesis by relaxing the broadband attenuation constraint to better attenuate the buffeting harmonics; as before, samples of the noise are still collected. If we obtain an admissible controller with $\gamma < \gamma_{max}$ (user-defined) and the resulting closed-loop plant in OLHP stable, we update the controller and proceed to state 3. If any of these conditions fail, restart state 2.

State 3

We now update the system to utilize our newly optimized controller. We restart our noise buffer and continue to collect noise samples until again we have collected the number required by section 5.4. Once we have a sufficient number of samples, we proceed to improve our model of $W_o(s)$ with a more recent version. Analysis of emprical noise tests of the buffeting showed a frequency drift of approximately 1 Hz. By consistently updating our model of the noise, we can maintain good active noise control. We stay in state 3 while $\hat{N}_{avg}$ remains above the threshold continuously remodelling the stochastic noise and updating our controller if an admissible result is found.

If at any time, the $\hat{N}_{avg}$ falls below our threshold, we return to state 1.

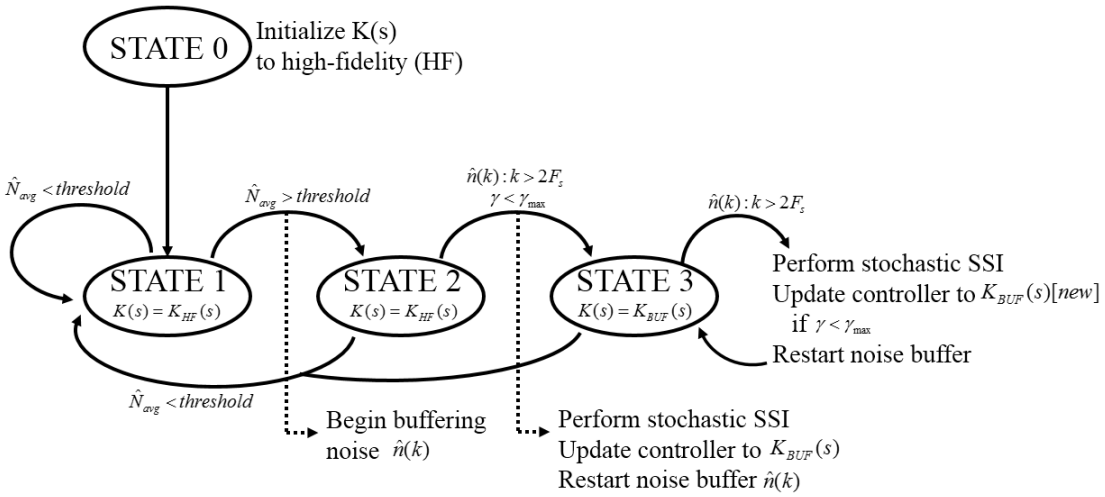

Fig. 6.8 State machine used to update controller

6.3 Simulations

6.3.1 Setup

We now proceed to setup the simulations to test the implementation of the state machine in combination with all stochastic subspace identification, noise estimator and controller optimization. Figure 6.9 shows the block diagram interconnecting all of the functional blocks. First, the system is tested with excitation from a musical reference, then we proceed to demonstrate the performance of pure active noise control. Issues with the amplifier are occasionally present and hence the saturation instruments in the block diagram are not always employed; the impact that this action has on simulation accuracy is acknowledged. Increasing the saturation limits to 700 V result in consistent behaviour; while this voltage level is likely too high for safe operation in a vehicle, an identical effect can be derived by improving the gain of the speaker which may be more feasible.

6.3.2 Simulation: music reference

The system is excited by a musical reference signal and the results shown in Figures 6.10a and 6.10b. In this test, the effectiveness of the algorithm is difficult to interpret in the time-domain since all signals contain both a reference signal and noise corruption; it is difficult to distinguish the components in the waveforms and hence we present the results in the

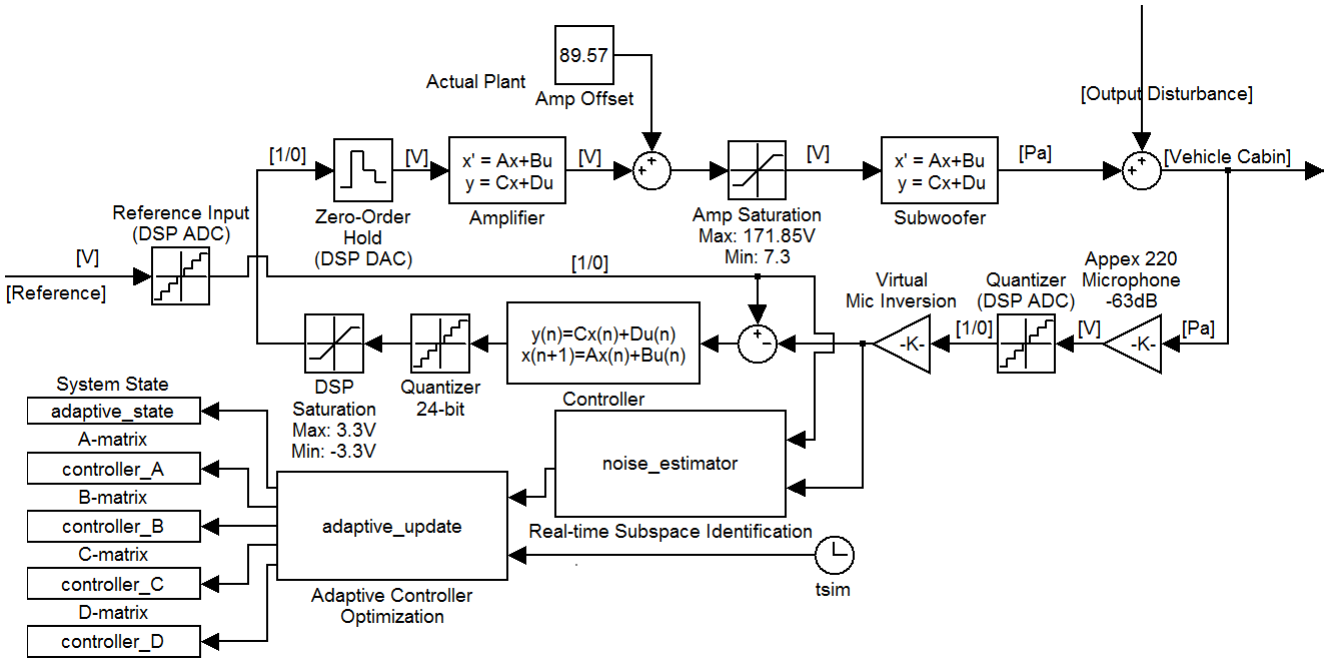

Fig. 6.9 Simulink model block diagram of control system with noise estimator and updating controller

frequency domain. Figure 6.10a shows the results of two simulations plotted on the same axes, both tests experience a low-amplitude ambient highway driving noise disturbance and an FFT of error signal shown. The signal denoted by ${}_{b}ctrl_{a}sim$ in represents the result of optimizing the controller for a buffeting disturbance but simulating it with only ambient noise. Conversely, ${}_{a}ctrl_{a}sim$ was optimized for ambient noise and high-fidelity acoustics and is simulated with ambient noise. This plot exemplifies why change our optimization criteria depending on the disturbance. A controller which has been incorrectly optimized for the wrong disturbance type, (e.g. ${}_{b}ctrl_{a}sim$) contains troughs in the error signal indicative of the harmonics of the buffeting used in its synthesis. Curve ${}_{a}ctrl_{a}sim$ was correctly optimized for low output disturbance and shows a flatter acoustic response.

In Figure 6.10b, we subject the system to an output disturbance containing high amplitude buffeting harmonics. Here, the same two controllers are plotted but their *relative* performance inverted. Now, the signal which was optimized for high quality musical reference tracking denoted by ${}_{a}ctrl_{b}sim$ shows a large error in the peaks associated with the modes in the output disturbance. The controller which was specifically tailored for this output disturbance, shown in the figure as ${}_{b}ctrl_{b}sim$ successfully attenuates the har-

monics of the buffeting. Notably, in higher frequencies, it is shown that the error in the buffeting-optimized controller exceeds that which was musically-optimized. This is an expected consequence of the waterbed effect. Compared to attenuation of the buffeting, this increase in high frequency noise is an acceptable trade-off.

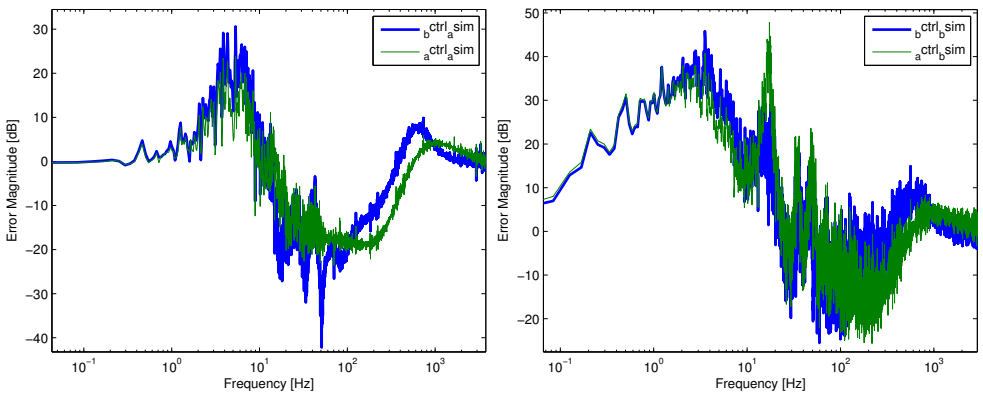

(a) (b)

Fig. 6.10 Error frequency response demonstrating controller performance under varying conditions of actual noise measurements in response to music reference. Signals prefixed with ${}_{b}ctrl$ are optimized for buffeting disturbance while ${}_{a}ctrl$ indicates high-fidelity optimization. (a) Simulated with ambient noise disturbance, (b) simulated with buffeting disturbance.

Simulation: pure ANC

Now we demonstrate the performance of the system in a pure noise cancellation environment. The system is given a zero-reference signal and begins with no output disturbance. At around 0.5s, we bombard the system with a low-amplitude disturbance before increasing the disturbance to simulate the full buffeting phenomenon at 2.3s. The buffeting remains present until the 11s mark, at which time we revert to a low noise level to simulate the closing of a window.

We begin by analyzing the results of the state machine progression to understand how the controller was updated as a function of time. For demonstrative purposes, stochastic subspace identification was carried out after only 1 second of buffeting and the controller synthesis attempted. Figure 6.11 shows the noise response which resulted from the stochastic SSI and was used in the $\mathcal{H}_\infty$ synthesis. As shown, the noise model at t=3.22, which

utilised only $F_s = 44100$ samples in the stochastic identification, caused the synthesis to fail; an admissible controller could not be found. The noise curve associated with this model is significantly higher in magnitude than that of the remaining curve which prevented convergence. The remaining controllers pass the test for an acceptable γ (typically 100) and allow for the update.

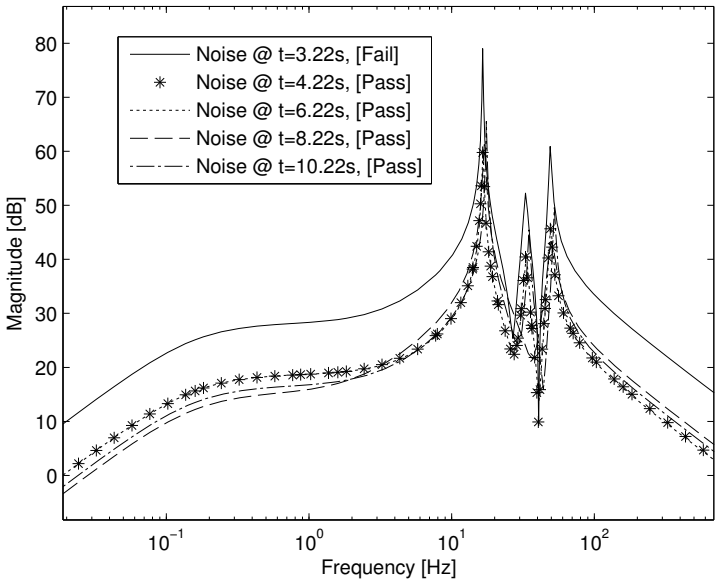

Fig. 6.11 Noise response used in controller optimization

The test is carried out using the empirical noise measurements from earlier experiments; here we see the performance of the control system in reaction to actual buffeting measurements from road tests. It is useful to examine more closely a section of the system's closed-loop sensitivity after the controller is updated, as shown in Figure 6.12. Measures of sensitivity at the various controller update times subject to the state machine operation are shown. The first and last curve indicate when the high-fidelity music controller was used; we see that there is a decrease in sensitivity which is associated with better broadband noise attenuation. When high volume noise is detected, we optimize the system with the disturbance model generated by the stochastic SSI which results in the less flat acoustic response. In Figure 6.12, we see from experimental data collected in the 2004 Toyota Matrix that there is a tendency for the harmonic peaks in the buffeting to drift with time. The dynamics of the time-varying noise signal are captured by each successive $W_o(s)$ model and incorporated directly into the noise cancelling scheme.

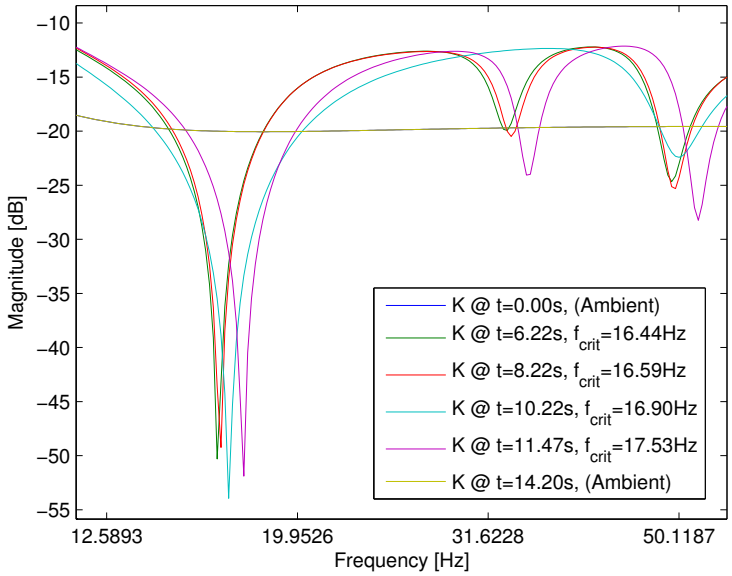

Fig. 6.12 A close-up of the evolving system sensitivity over time in reaction to actual buffeting noise from road tests, the resonant frequency of the buffeting changes over time with the controller adapting to the dynamic harmonic

We now present the time domain results from the pure acoustic noise attenuation. The full scale of the simulation is shown in Figure 6.13 where we see the system's output superimposed over the output disturbance. Green vertical bars indicate successful updates to the controller while blue vertical bars indicate a failed update. At 3.1s, the attempted update to the controller fails to identify an admissible controller which results in a stable closed-loop plant, hence there is no change to the controller in operation. At 4.1s, the optimization is re-attempted using a longer sample length in the stochastic identification. This optimization is successful and the controller is updated. Every two seconds subsequent to this, a new controller is synthesized that better matches the harmonics in the disturbance. At around 11.5s, shortly after the window has closed, the noise level measured by $\hat{N}_{avg}$ falls below the threshold and the system reverts to high-fidelity controller.

A close-up of the controller transitions is shown in Figures 6.14 and 6.15. In Figures 6.14, we see that buffeting harmonics continue to be significant in the system output until 4.22s at which time the controller is updated. A discontinuity is introduced at the transition, this is perceived by a user as an undesirable "popping" sound; additional work is required to ease the transitionary period. Since the states of the updated controller are uninitialized,

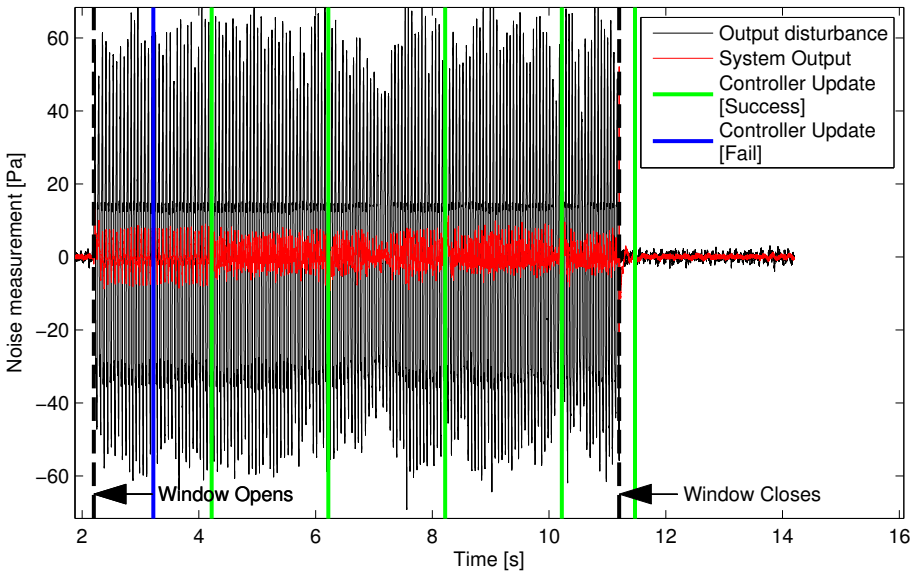

Fig. 6.13 Performance of adaptive controller in vehicle noise cancellation, 100 km/h simulation, 0-input reference signal

the controller fails to stay in phase with the existing pulse. However, once the transients of the transition diminish, the rejection of the output disturbance is achieved. The addition of some high frequency noise is also observed.

A close-up of a second transition is shown at 10.22s in Figure 6.14 which represents a controller re-optimization with a new model of $W_o(s)$. Again, after the transients diminish, we see an improvement in the rejection of the harmonics.

Simultaneously implementation of all of the algorithms discussed in this thesis was not attempted on the Freescale hardware platform. It is not known whether the added computational complexity will exceed the limitations of what can be achieved in real-time. However, this thesis seeks to demonstrate a technique for incorporating noise models directly into the $\mathcal{H}_\infty$ optimization to improve disturbance rejection.

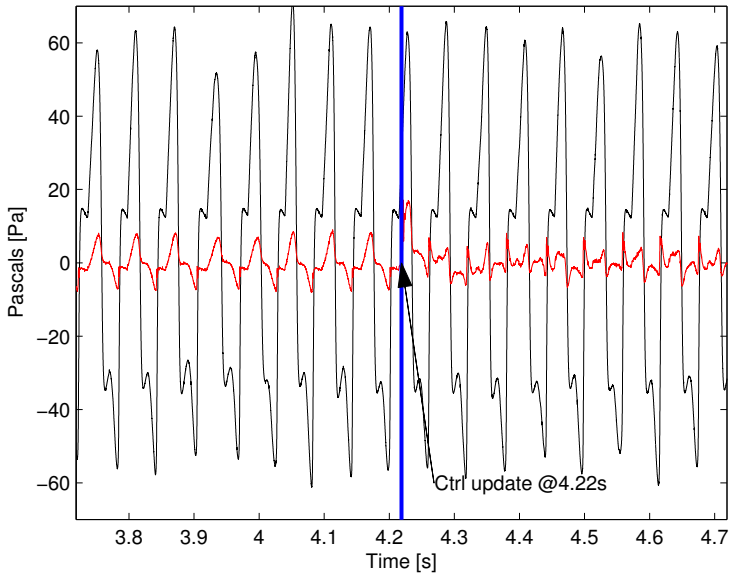

Fig. 6.14 Time response of adaptive control taking effect, disturbance change from ambient highway noise to buffeting at 2.3s with updated controller engaging at 4.22s

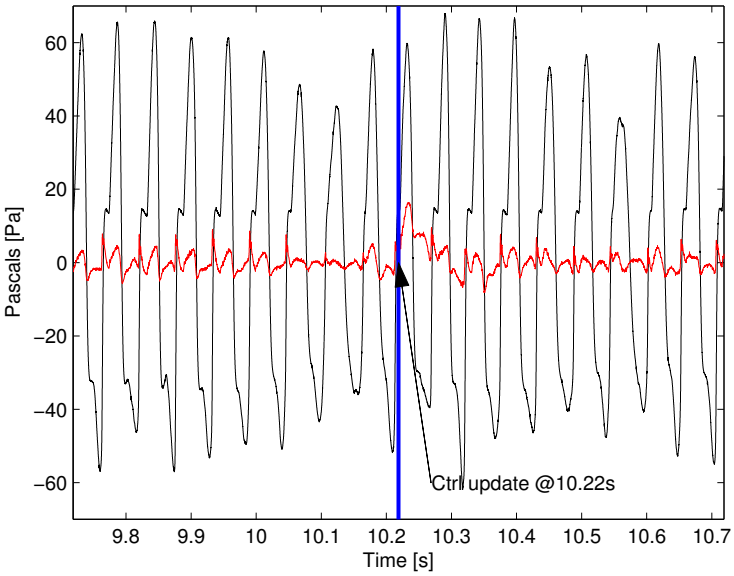

Fig. 6.15 Adaptive controller updating after detecting a shift in noise characteristics, buffeting harmonic drift compensated.

Chapter 7

Conclusions and Future Work

In this thesis, we have presented a technique for controlling the operation of a piezoelectrically oscillated windshield which aims to replace traditional low-frequency speakers within automotive vehicles.

Deterministic subspace identification, which is typically used strictly for theoretical demonstration due to its requirement from completely noise-free measurements, is used to model the laboratory apparatus. After sine wave sweeping our laboratory apparatus in a series of tests and configurations, we perform a frequency by frequency high-order bandpass on the I/O signals to isolate specifically the frequency of oscillation. Applying the filter to both waveforms negated its impact on the magnitude and phase relation between the signals. With most interference removed, we are then able to perform zero-cross detection on the signals to compute their phase while the gain is determined from the change their respective RMS. Synthetic I/O signals are then generated from the magnitude-phase pairs which are intended to be noise free. The deterministic subspace algorithm works well in yielding a model which closely matches the empirical results post-filtering. However, large phase discontinuities resulted from errors in the zero-cross detection introduced undesirable artefacts into the system models. Combined deterministic-stochastic subspace identification is a technique which allows for the identification of plant matrices without requiring purely noise-free data. In future work, an exploration of these algorithms, such as those presented by Van Overschee and De Moor in [38], may result in more accurate plants that do not require the special processing to remove undesirable NMP zeros and unstable poles. This will result in a more realistic plant model and better control system. By removing all

NMP zeros which must be present in acoustic cavities, the realism of the plant was reduced drastically- even despite our attempt to compensate with lead-lag filters.

Stochastic subspace identification performed on empirical noise measurements produced models which could be incorporated directly into the $\mathcal{H}_\infty$ synthesis serving as estimates of the spectral densities associated with the output disturbance. An insufficiently thorough use of the stochastic subspace identification techniques results in the necessity to incorporate a gain value to match the units of the noise models. It is believed that this gain value, and its apparent arbitrary value, may have unforeseen consequences in the subsequent modelling and controller design. It is believed that better use of the covariance of the forward innovation model in [38] will improve the unit accuracy. It would be beneficial to obtain disturbance models which did not require such scaling before attempting to perform controller synthesis.

Our noise estimator, which streamed the data required by the stochastic identification block, uses only fixed estimates of the plant matrices. No uncertainty is incorporated in their value in this analysis nor is any filtering performed on the estimate. The use of a Kalman filter or other algorithms may improve the accuracy of the noise estimates.

Weighting functions derived from models of ideal transmission behaviour of speakers are used to create constraints on the infinity norm of the system's sensitivity to effectively flatten the acoustic response of the speaker. Constraints in the amplifier saturation limits and volume of the speaker resulted in difficulty performing the $\mathcal{H}_\infty$ synthesis of an admissible controller. These constraints were relaxed by assumptions that are deemed reasonable but the overall accuracy of simulations would benefit from identifying more closely realistic parameters.

The error weighting function is shaped selectively based on the particular control objective that we seek to accomplish. When the ambient noise within the vehicle is low, we insist on broadband noise attenuation to improve the acoustic linearity of the speaker. Window buffeting is introduced when a single window is opened by some amount. In the face of this phenomenon, we sacrifice broadband attenuation in place of more aggressive attenuation of the characteristic harmonics in the buffeting signal to more effectively cancel the hammering tone. Model order and controller order reduction are not performed in this thesis. To this end, the feasibility to implement the algorithms used in this thesis onboard a DSP is only briefly discussed. In future work, a detailed analysis on computation times may suggest that a real-time operating system is required on the DSP to thread the ex-

ecution of the controller, controller synthesis and modelling. An FPGA implementation might allow for a low-cost means to tailor soft processors to execute the operational tasks in parallel.

Limitations caused by Bode's sensitivity integral introduce the waterbed effect which cause noise in frequency bands outside that which we control. Typically pushed to higher frequencies by the waterbed effect, an increased sensitivity manifests as undesirable static noise. A more aptly tuned error weighting function might be able to shift the "bump" associated with the necessary increase in sensitivity to *below* the audible spectrum of human hearing. Oscillations in this band would be perceivable by touch to human observers but could not be heard.

Audible human speech within the vehicle generally exists outside of this band. While the fundamental mode in adult males is 130 Hz and 210 Hz in adult females on average [57], the majority of their vocal harmonics exists in the frequency range above this band. The presence of these and other *internal* disturbances reinforces the strict requirement to limit the control actuation to frequencies in the band below this level. In future work, it is postulated how one may incorporate a high order filter into the feedback sensor to sharply attenuate frequencies above 200 Hz to prevent them from entering the control loop. While the incorporation of such a filter in the $\mathcal{H}_\infty$ synthesis would significantly increase the order of the system, it would be desirable to study the effect on stability and performance by adding such a filter after the synthesis has completed.

Stability theorems for adaptive controllers are not included in this thesis. A detailed stability analysis on the algorithms which we presented would provide a more complete understanding of the system's behaviour and is crucial before implementation in a vehicle.

A robust control theory treatment of the problem tackled in this thesis would allow for a more quantitative estimate on the impact of narrowing the uncertainty of the output disturbance. Uncertainties in the plant model should also be incorporated to ensure both robust stability and performance.

While the intent of this thesis is to develop a system for implementation on-board a digital signal processor, experimental verification of the thesis results is not demonstrated here. The roadmap to such an implementation is explained in detail including the state-machine model and simulation demonstration; however, the feasibility of such computationally heavy system identification and controller synthesis could not be determined. For additional information to aid the reader in implementation, the author recommends a review of the

techniques employed by Pourboghrat in [51] where the use of real-time, recursive subspace identification carried out on a digital signal processor. It is the intent of future work to incorporate such recursive subspace identification algorithms, first demonstrated in [58] to better demonstrate the practicality of the algorithms presented in this thesis.

References

[1] Mats Gustavsson, "Device for actuating a membrane and a vehicle comprising a device for actuating a membrane," U.S. Patent 7 236 602, Jun. 26, 2007.

[2] J. R. Phillips, "Piezoelectric Technology Primer," CTS Wireless Components, Tech. Rep.

[3] L. Weiping, C. Zhifu, and X. Zhi, "Analysis of vehicle side window buffeting characteristics and suppression using cfd," in *Computer-Aided Industrial Design Conceptual Design, 2009. CAID CD 2009. IEEE 10th International Conference on*, Nov. 2009, pp. 846–851.

[4] B. Boulet and Y. Duan, "The fundamental tradeoff between performance and robustness - a new perspective on loop shaping - classic control revisited part ii," *Control Systems, IEEE*, vol. 27, no. 3, pp. 30–44, June 2007.

[5] T. J. Cox and P. D'antonio, *Acoustic absorbers and diffusers: theory, design and application*. CRC PressI Llc, 2009.

[6] B. Rudzyn, M. Fisher, N. Chong-White, J. Mejia, and H. Dillon, "Active noise control core technology," Macquarie Park, New South Wales, Australia.

[7] S. Kuo and D. Morgan, "Active noise control: a tutorial review," *Proceedings of the IEEE*, vol. 87, no. 6, pp. 943–973, Jun 1999.

[8] B. Widrow and J. M.E, Hoff, "Adaptive switch circuits," *IRE WESCON Convention Record*, pp. 96–104, August 1960.

[9] B. Widrow and S. D. Stearns, "Adaptive signal processing," *Englewood Cliffs, NJ, Prentice-Hall, Inc., 1985, 491 p.*, vol. 1, 1985.

[10] B. Widrow, M. Lehr, F. Beaufays, E. Wan, and M. Bilello, "Adaptive signal processing," *Proceedings of the World Conference on Neural Networks*, July 1993.

[11] B. Farhang-Boroujeny, *Adaptive Filters Theory and Applications*. John Wiley & Sons, January 1999.

[12] B. Widrow, D. Shur, and S. Shaffer, "On adaptive inverse control," *Record of the Fifteenth Asilomar Conference on Circuits, Systems and Computers, Proc. 15th Asilomar Conf.*, p. 185189, November 1981.

[13] B. Widrow and S. D. Stearns, "Adaptive signal processing," *Englewood Cliffs, NJ, Prentice-Hall, Inc., 1985, 491 p.*, vol. 1, 1985.

[14] B. J. Kim and D. C. Swanson, "Linear independence method for system identification/secondary path modeling for active control," *The Journal of the Acoustical Society of America*, vol. 118, no. 1452, 2005.

[15] S. Popovich, D. Melton, and M. Allie, "New adaptive multichannel control systems for sound and vibration," in *INTER-NOISE and NOISE-CON Congress and Conference Proceedings*, vol. 1992, no. 3. Institute of Noise Control Engineering, 1992, pp. 405–408.

[16] A. Efron and L. C. Han, "Wide-area adaptive active noise cancellation," *Circuits and Systems II: Analog and Digital Signal Processing, IEEE Transactions on*, vol. 41, no. 6, pp. 405–409, Jun 1994.

[17] S. Kuo, C. Holmes, and P. Mallela, "Integrated automotive signal processing and audio system," *Consumer Electronics, IEEE Transactions on*, vol. 39, no. 3, pp. 522–532, Jun 1993.

[18] M. Akhtar and W. Mitsuhashi, "A modified normalized fxlms algorithm for active control of impulsive noise," in *18th European Signal Processing Conference (EUSIPCO-2010)*, 2010.

[19] J. Cheer and S. Elliott, "Modal and multichannel feedback control of road noise in a car," Institute of Sound and Vibration Research, University of Southampty, Tech. Rep., June 2012.

[20] T. J. Sutton, S. J. Elliott, A. M. McDonald, and T. J. Saunders, "Active control of road noise inside vehicles," *Noise Control Engineering Journal*, vol. 42, no. 4, pp. 137–148, 1994.

[21] S. J. Elliott and P. A. Nelson, "Active noise control," *Signal Processing Magazine, IEEE*, vol. 10, no. 4, pp. 12–35, 1993.

[22] J. Garcia-Bonito and S. Elliott, "Local active control of diffracted diffuse sound fields," *The Journal of the Acoustical Society of America*, vol. 98, p. 1017, 1995.

[23] J. Hong, J. Akers, R. Venugopal, M.-N. Lee, A. G. Sparks, P. Washabaugh, and D. Bernstein, "Modeling, identification, and feedback control of noise in an acoustic

duct," *Control Systems Technology, IEEE Transactions on*, vol. 4, no. 3, pp. 283–291, May 1996.

[24] Z. Yang, "Design of active noise control using feedback control techniques for an acoustic duct system," in *Robotics, Automation and Mechatronics, 2004 IEEE Conference on*, vol. 1, Dec, pp. 467–472 vol.1.

[25] R. Boonen and P. Sas, "Stability improvement for feedback noise control in ducts using a time delay compensator," in *Proceedings of the 23rd International Seminar on Modal Analysis*, vol. 1. KU Leuven; 1998, 2001, pp. 9–14.

[26] H. Sano, T. Inoue, A. Takahashi, K. Terai, and Y. Nakamura, "Active control system for low-frequency road noise combined with an audio system," *Speech and Audio Processing, IEEE Transactions on*, vol. 9, no. 7, pp. 755–763, Oct 2001.

[27] I. Stothers, T. Saunders, A. McDonald, and S. Elliott, "Adaptive feedback control of sun roof flow oscillations," *Proceedings Institute of Acoustics*, vol. 15, pp. 383–383, 1993.

[28] G. Zames, "Feedback and optimal sensitivity: Model reference transformations, multiplicative seminorms, and approximate inverses," *Automatic Control, IEEE Transactions on*, vol. 26, no. 2, pp. 301–320, April 1981.

[29] I. M. Horowitz, *Synthesis of feedback systems*. Academic Press New York, 1963, vol. 1663.

[30] A. Tannenbaum, "Feedback stabilization of linear dynamical plants with uncertainty in the gain factor," *International Journal of Control*, vol. 32, no. 1, pp. 1–16, 1980.

[31] J. C. Doyle, "Analysis of feedback systems with structured uncertainties," *Control Theory and Applications, IEE Proceedings D*, vol. 129, no. 6, pp. 242–250, November 1982.

[32] L. Xie and C. E. De Souza, "Robust h infin; control for linear systems with norm-bounded time-varying uncertainty," *Automatic Control, IEEE Transactions on*, vol. 37, no. 8, pp. 1188–1191, Aug 1992.

[33] V. A. Ugrinovskii, "Robust H_∞ infinity control in the presence of stochastic uncertainty," *International Journal of Control*, vol. 71, no. 2, pp. 219–237, 1998. [Online]. Available: http://www.tandfonline.com/doi/abs/10.1080/002071798221849

[34] B. Sayyarrodsari, J. P. How, B. Hassibi, and A. Carrier, "An $\mathcal{H}_\infty$-optimal alternative to the fxlms algorithm," in *American Control Conference, 1998. Proceedings of the 1998*, vol. 2. IEEE, 1998, pp. 1116–1121.

[35] B. Rafaely and S. Elliott, "$\mathcal{H}_2$ / $\mathcal{H}_\infty$ active control of sound in a headrest: design and implementation," *Control Systems Technology, IEEE Transactions on*, vol. 7, no. 1, pp. 79–84, Jan 1999.

[36] T. Knudsen, *Subspace Identification: Reducing Uncertainty on the Stochastic Part.* Aalborg University, Department of Control Engineering, 2001.

[37] K. De Cock and B. De Moor, "Subspace identification methods," in *UNESCO Encyclopedia of Life Support Systems, Unbehauen HD (ed.).* Eolss Publishers Co., Ltd., 2003, vol. 1, no. 3, ch. Control systems, robotics and automation, pp. 933–979.

[38] P. van Overschee and L. de Moor, *Subspace identification for linear systems: theory, implementation, applications.* Kluwer Academic Publishers, 1996, no. v. 1.

[39] S. J. Qin, "An overview of subspace identification," *Computers & chemical engineering*, vol. 30, no. 10, pp. 1502–1513, 2006.

[40] M. Abdelghani and M. Friswell, "Estimation of modal parameter uncertainties using stochastic subspace algorithms," *Fourth International Conference on Advances in Mechanical Engineering and Mechanics*, pp. 16–18, Sousse, Tunisia 2008.

[41] M. Dohler, X.-B. Lam, and L. Mevel, "Uncertainty quantification for stochastic subspace identification on multi-setup measurements," in *Decision and Control and European Control Conference (CDC-ECC), 2011 50th IEEE Conference on*, Dec. 2011, pp. 6451–6456.

[42] H. Balini, I. Houtzager, J. Witte, and C. W. Scherer, "Subspace identification and robust control of an amb system," in *American Control Conference (ACC), 2010.* IEEE, 2010, pp. 2200–2205.

[43] S. Adachi and H. Sano, "Application of two-degree-of-freedom type active noise control using imc to road noise inside automobiles," in *Decision and Control, 1996., Proceedings of the 35th IEEE Conference on*, vol. 3, December 1996, pp. 2794–2795 vol.3.

[44] A. Electronics, "Apex 220 omnidirectional measurement and test microphone," Web., APEX Electronics, Niagara Falls, NY. [Online]. Available: http://www.apexelectronics.com/files/products/Apex220/Apex220-om.pdf

[45] B. Laurence, "Acoustivision - proposed hardware development platforms," McGill University, Tech. Rep., January 2011.

[46] B. Boulet, "Linear systems," University Lecture, 2010.

[47] J. C. Willems, "From time series to linear systempart i: vol. 22, no. 5, pp. 561-580, part ii: vol. 22, no. 6, pp. 675-694 part iii: vol. 23, no. 1, pp. 87-115," *Automatica*, 1986.

[48] M.-P. Jolicoeur, "Model identication of a car suspension testbed for robust vibration control," M.Eng. thesis, McGill University, Department of Electrical Engineering, Aug. 1995.

[49] B. Peeters and G. De Roeck, "Reference-based stochastic subspace identification for output-only modal analysis," *Mechanical Systems and Signal Processing*, vol. 13, no. 6, pp. 855–878, 1999.

[50] B. Boulet, *Fundamentals of Signals and Systems*. Charles River Media: Thomson Learning Inc., 2006.

[51] H. Pongpairoj and F. Pourboghrat, "Real-time optimal control of flexible structures using subspace techniques," *Control Systems Technology, IEEE Transactions on*, vol. 14, no. 6, pp. 1021–1033, 2006.

[52] M. Morari and E. Zafiriou, *Robust process control*. Morari, 1989.

[53] B. Boulet, "Robust control systems," University Lecture, 2011.

[54] B. A. Francis and W. M. Wonham, "The internal model principle of control theory," *Automatica*, vol. 12, no. 5, pp. 457–465, 1976.

[55] K. Glover and J. C. Doyle, "State-space formulae for all stabilizing controllers that satisfy an $\mathcal{H}_\infty$-norm bound and relations to relations to risk sensitivity," *Systems & Control Letters*, vol. 11, no. 3, pp. 167–172, 1988.

[56] P. A. Iglesias, "Tradeoffs in linear time-varying systems: an analogue of bode's sensitivity integral," *Automatica*, vol. 37, no. 10, pp. 1541–1550, 2001.

[57] H. Traunmüller and A. Eriksson, "The frequency range of the voice fundamental in the speech of male and female adults," 1993.

[58] T. Gustafsson, M. Lovera, and M. Verhaegen, "A novel algorithm for recursive instrumental variable based subspace identification," in *Decision and Control, 1998. Proceedings of the 37th IEEE Conference on*, vol. 4, 1998, pp. 3920–3925 vol.4.